

Observational Characteristics of Accretion onto Black Holes

C. Done

Department of Physics, University of Durham, South Road, Durham, DH1 3LE:

chris.done@durham.ac.uk

1

Observational Characteristics of Accretion onto Black Holes

1.1 Abstract

These notes resulted from a series of lectures at the IAC winter school. They are designed to help students, especially those just starting in subject, to get hold of the fundamental tools used to study accretion powered sources. As such, the references give a place to start reading, rather than representing a complete survey of work done in the field.

I outline Compton scattering and blackbody radiation as the two predominant radiation mechanisms for accreting black holes, producing the hard X-ray tail and disc spectral components, respectively. The interaction of this radiation with matter can result in photo-electric absorption and/or reflection. While the basic processes can be found in any textbook, here I focus on how these can be used as a toolkit to interpret the spectra and variability of black hole binaries (hereafter BHB) and Active Galactic Nuclei (AGN). I also discuss how to use these to physically interpret real data using the publicly available XSPEC spectral fitting package (Arnaud et al 1996), and how this has led to current models (and controversies) of the accretion flow in both BHB and AGN.

1.2 Fundamentals of accretion flows: observation and theory

1.2.1 Plotting Spectra

Spectra can often be (roughly) represented as a power law. This can be written as a differential photon number density (photons per second per square cm per energy band) as $N(E) = N_0 E^{-\Gamma}$ where Γ is photon index. The energy flux is then simply $F(E) = EN(E) = N_0 E^{-(\Gamma-1)} = N_0 E^{-\alpha}$ where $\alpha = \Gamma - 1$ is energy index.

Power law spectra are broad band, i.e. the emission spans many decades in energy. Thus in general we plot logarithmically, in $\log E$, with $d \log E$ rather than dE as the constant. The number of photons per bin is $N(E)dE = N(E)EdE/E =$

$EN(E)d\log E = F(E)d\log E$. Thus, somewhat counter-intuitively, plotting $F(E)$ on a logarithmic energy scale shows the *number* of photons rather than flux.

Similarly, energy per bin is $F(E)dE = F(E)EdE/E = EF(E)d\log E$. Thus to see the energy at which the source luminosity peaks on a logarithmic frequency scale means we have to plot $\log EF(E)$ ($= \nu F(\nu)$) versus $\log E$. In these units, hard spectra have $\Gamma < 2$ so peak at high energies. Soft spectra have $\Gamma > 2$ and peak at low energies. Flat spectra with $\Gamma = 2$ means equal power per decade. These are illustrated in Fig. 1.1.

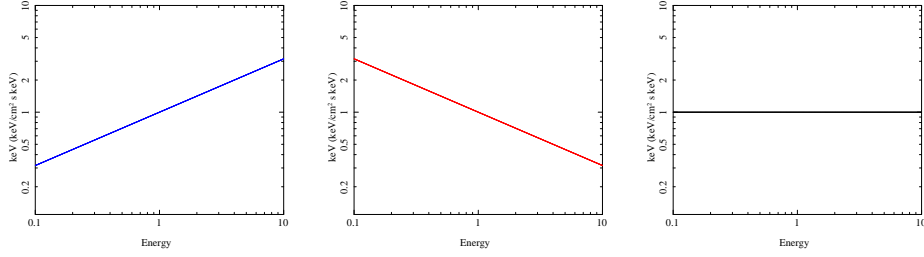


Figure 1.1 The $\nu f(\nu)$ spectra of a power law with photon index Γ of 1.5, 2.5 and 2.0. This representation makes it clear that the power output peaks at high energies for hard spectra ($\Gamma < 2$) while it peaks at low energies for soft spectra ($\Gamma > 2$).

One other very common way for spectra to be plotted is in counts per second per cm^2 , $C(E)$. This is *not* the same as $N(E)$, the counts refer to number of photons *detected* not emitted. Such spectra show more about the detector than the intrinsic spectrum as these are convolved with the detector response giving $C(E) = \int N(E_0)R(E, E_0)dE_0$ where $R(E, E_0)$ is the detector response i.e. the probability that a photon of input energy E_0 is detected at energy E . Instrument responses for X-rays are generally complex so the spectra are generally analysed in counts space, by convolving models of the intrinsic spectrum through the detector response and minimizing the difference between the predicted and detected counts to derive the best fit model parameters. While such 'counts spectra' constitute the basic observational data, they do not give a great deal of physical insight. Deconvolving these data using a model to plot them in $\nu f(\nu)$ space is strongly recommended i.e. in XSPEC using the command IPLOT EEUF.

1.2.2 Plotting variability

Plotting variability is analogous to plotting spectra. A light-curve, $I(t)$, spanning time T , with points every Δt can be decomposed into a sum of sinusoids:

$$I(t) = I_0 + \sum_{i=1}^N A_i \sin(2\pi\nu_i t + \phi_i)$$

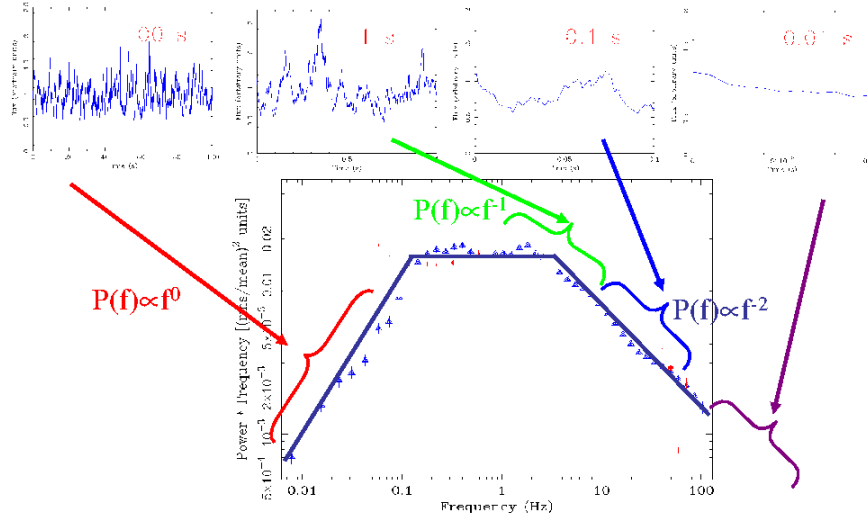


Figure 1.2 The lower panel shows the power spectrum of a lightcurve from a low/hard state of Cyg X-1. The upper panels show segments of the lightcurve spanning timescales of 100s, 1s, 0.1s and 0.01s, respectively. These are each normalized to their mean, so it is easy to see that the fractional variability is largest in the 1s light-curve, and that this is what the power spectrum measures. Figure courtesy of P. Uttley. (Uttley 2007)

where I_0 is the average flux over that timescale, $\nu_i = i/T$ with $i = 1, 2, \dots, N$ and $N = T/(2\Delta t)$. This is more useful when normalized to the average, giving the fractional change in intensity $I(t)/I_0 = 1 + \sum (A_i/I_0) \sin(2\pi\nu_i t + \phi_i)$. The power spectrum $P(\nu)$ is $(A_i/I_0)^2$ versus ν_i , and the integral $\int P(\nu) d\nu = (\sigma/I)^2$ i.e. the squared total r.m.s. variability of the lightcurve.

Similar to the energy spectra, the power spectrum is generally broad band so is plotted logarithmically. Then the total variability power in a bin is $P(\nu)d\nu = P(\nu)\nu d\nu/\nu = \nu P(\nu)d \log \nu$. Thus, similarly to spectra, a peak in $\nu P(\nu)$ versus $\log \nu$ shows the frequency at which the variability power peaks, so this is the more physical way to plot power spectra.

The data often show power-law power spectra, with $P(\nu) \propto \nu^0$ on long timescales breaking to ν^{-1} at a low frequency break ν_b and then breaking again to ν^{-2} at a

high frequency break ν_h . This is termed band limited noise or flat-top noise, where the 'flat-top' has $P(\nu) \propto \nu^{-1}$ as this has equal variability power per decade.

Fig.1.2 illustrates this for data from a low/hard state (see section 1.2.4) in Cyg X-1. The light-curves are shown over different timescales, T . These are all normalized to their mean, so it is easy to see from the light-curves that the fractional variability is very low on timescales shorter than 0.01 s. At longer timescales the fractional variability increases, then remains constant for 1-10 s and then drops again.

1.2.3 Spectra and Variability of the Shakura-Sunyaev disc

The underlying physics of a Shakura-Sunyaev accretion disc can be illustrated in a very simple derivation just conserving energy (rather than the proper derivation which conserves energy and angular momentum).

A mass accretion rate \dot{M} spiraling inwards from R to $R - dR$ liberates potential energy at a rate $dE/dt = L_{pot} = (GM\dot{M}/R^2) \times dR$. The virial theorem says that only half of this can be radiated, so $dL_{rad} = GM\dot{M}dR/(2R^2)$. If this thermalises to a blackbody then $dL = dA\sigma_{SB}T^4$ where σ_{SB} is the Stephan-Boltzman constant and area of the annulus $dA = 2 \times 2\pi R \times dR$ (where the factor 2 comes from the fact that there is a top and bottom face of the ring). Then the luminosity from the annulus $dL_{rad} = GM\dot{M}dR/(2R^2) = 4\pi R \times dR\sigma_{SB}T^4$ or $\sigma_{SB}T^4(R) = GM\dot{M}/8\pi R^3$. This is only out by a factor $3(1 - (R_{in}/R)^{1/2})$ which comes from a full analysis including angular momentum (see H. Spruit in these proceedings).

Thus the spectrum from a disc is a sum of blackbody components, with increasing temperature and luminosity emitted from a decreasing area as the radius decreases. The peak luminosity and temperature then comes from R_{in} (modulo the corrections for the inner boundary condition). Using the very approximate treatment above, the total total luminosity of the disc $L_{disc} = GM\dot{M}/(2R_{in})$ so substituting for $GM\dot{M}$ gives $\sigma_{SB}T^4(R) = R_{in}L_{disc}/4\pi R^3 \propto L_{disc} \times (R_{in}/R) \times 1/(4\pi R^2)$. So $\sigma_{SB}T_{max}^4 = \sigma_{SB}T(R_{in}) = L_{disc}/(4\pi R_{in}^2)$, giving an observational constraint on R_{in} if we can measure T_{max} and L_{disc} . This is important as R_{in} is set by General Relativity at the last stable orbit around the black hole, which is itself dependent on spin. Angular momentum, J , is typically a mass, times a velocity, times a size scale. The smallest size scale for a black hole is that of the event horizon, which is always larger than $R_g = GM/c^2$, and the fastest velocity is the speed of light. Thus $|J| < McGM/c^2$, or spin-per-unit mass, $|J|/M = a_*GM/c$, where $a_* \leq 1$. The last stable orbit is at $6 R_g$ for a zero spin ($a_* = 0$: Schwarzschild) black hole, decreasing to $1 R_g$ for a maximally rotating Kerr black hole for the disc co-rotating with the black hole spin ($a_* = 1$), or $9 R_g$ for a counter-rotating disc ($a_* = -1$). Thus to convert the observed emission area to spin we need to know the

mass of the black hole so we can put the observed inner radius into gravitational radii $r_{in} = R_{in}/R_g$, giving us a way to observationally measure black hole spin.

In XSPEC, a commonly used model for the disc is DISKBB. This assumes that $T^4 \propto r^{-3}$ i.e. has no inner boundary condition. It is adequate to fit the high energy part of the disc spectrum i.e. the peak and Wien tail, but the derived normalization needs to be corrected for the lack of boundary condition. It also assumes that each radius emits as a true blackbody, which is only true if the disk is effectively optically thick to absorption at all frequencies. Free-free (continuum) absorption drops as a function of frequency, so the highest energy photons from each radii are unlikely to thermalize. This forms instead a modified (or diluted) blackbody, with effective temperature which is a factor f_{col} (termed a colour temperature correction) higher than for complete thermalization. The full disk spectrum is then a sum of these modified blackbodies, but this can likewise be approximately described by a single colour temperature correction to a 'sum of blackbodies' disk spectrum (Shimura & Takahara 1995), giving rise to a further correction to the DISKBB normalization. The final factor is that the emission from each radius is smeared out by the combination of special and general relativistic effects which arise from the rapid rotation of the emitting material in a strong gravitational field (Cunningham 1975, see section 1.5.4). Again, these corrections can be applied to the DISKBB model (e.g. Kubota et al 2001; Gierlinski & Done 2004a), but are only easily available as tabulated values for spin 0 and 0.998 in Zhang et al (1997). Hence a better approach is to use KERRBB, which incorporates the stress-free boundary condition and relativistic smearing for any spin (Li et al 2005) for a given colour temperature correction factor. An even better approach is to use BHSPEC, which calculates the intrinsic spectrum from each radius using full radiative transfer through the disc atmosphere, including partially ionized metal opacities, rather than assuming a colour temperature corrected blackbody form (Davis et al 2005). This imprints atomic features onto the emission from each radius, distorting the spectrum from the smooth continuum as produced by KERRBB (Done & Davis 2008, Kubota et al 2010).

To zeroth order, the emitted spectrum does not require any assumptions about the nature of the viscosity, parameterized by α by Shakura & Sunyaev (1973). However, variability is dependent on this, as variability in the emitted spectrum requires that the mass accretion rate through the disc changes. Material can only fall in if its angular momentum is transported outwards via 'viscous' stresses, now known to be due to the magneto-rotational instability (MRI, see J. Hawley lecture notes in this proceedings). The viscous timescale, $t_{visc} \approx \alpha^{-1} (H/R)^{-2} t_{dyn}$ where H is the vertical scale height of the disc and $t_{dyn} = 2\pi R_g (r^{3/2} + a_*)/c$ is the dynamical (orbital) timescale which is ~ 5 ms for a Schwarzschild black hole of $10M_\odot$.

Modeling the observed variability of the disc gives an estimate for $\alpha = 0.1$ (King, Pringle & Livio 2007), though current simulations of the MRI gives stresses which are an order of magnitude lower than this (see J. Hawley lecture notes in this proceedings).

The disc models give a geometrically thin solution $H/R \sim 0.01$, so the very fastest variability from changes in mass accretion rate at the innermost edge are 100,000 times longer than the dynamical timescale. Thus accretion discs in black hole binaries (hereafter BHB) should only vary on timescales longer than a few hundred seconds.

1.2.4 Observed Spectra and Power Spectra of Black Hole Binaries

Disc dominated states

The mass accretion rate through the entire disc in BHB can vary over weeks-months-years, triggered by the disk instability (see R. Hynes in these proceedings or Done, Gierlinski & Kubota 2007, hereafter DGK07). This means that a single object (with constant distance, inclination and spin) can map out how the spectrum changes as a function of luminosity as shown in Fig. 1.3.

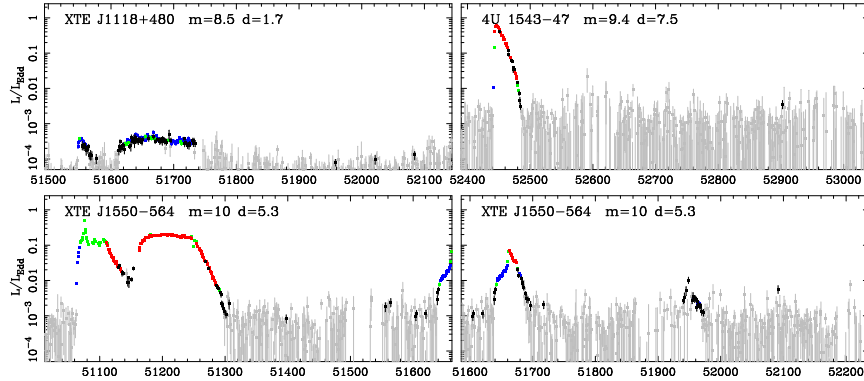


Figure 1.3 The long term All Sky Monitor RXTE lightcurves of some transient BHB (DGK07). In the electronic version these are colour coded to indicate their spectral shape (see Fig. 1.5) with low/hard in blue, high/soft as red and very high state in green.

Fig. 1.4a shows that these can indeed show spectra which look very like the simple accretion disc models described above (section 1.2.3). This disc emission also shows very little rapid variability on timescales of less than a few hundred seconds, as expected (Churazov et al 2001). Collating disc spectra on longer timescales at different \dot{m} gives $L_{disc} \propto T_{max}^4$ (Fig. 1.4b), clear observational evidence for a constant size-scale inner radius to the disc despite the large change in mass accretion

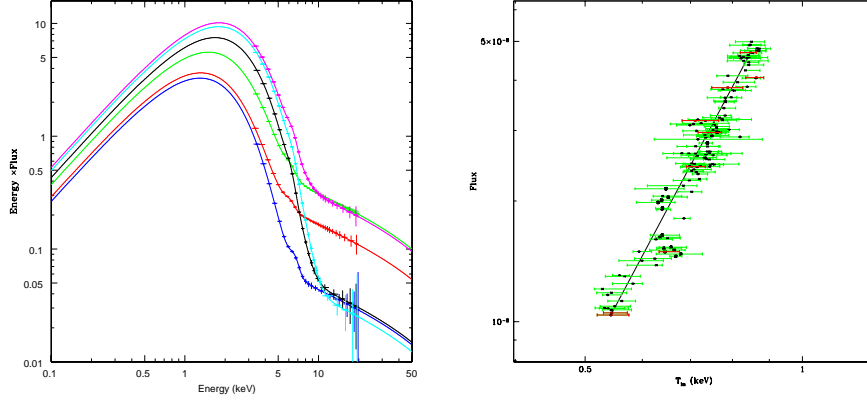


Figure 1.4 a) A selection of disc dominated spectra from the transient BHB GX339-4 b) The disc flux versus its temperature derived from fits to all the disc dominated data. The line shows the $L_{disc} \propto T_{max}^4$ relation expected from a constant size scale for the inner radius of the disc (Kolehmainen & Done 2010)

rate. This is exactly as predicted for the behaviour at the last stable orbit, and is a key test of Einstein's gravity in the strong field limit. Indeed, given how close the last stable orbit is to the event horizon ($r = 6$ compared to the horizon at $r = 2$ for a Schwarzschild black hole), this represents almost the strongest gravitational field we could ever observe.

Folding in all the required corrections (see above) allows us to measure this fixed size-scale and translate it into a measure of spin if there are good system parameter estimates (see R. Hynes in these proceedings). To date, all objects which show convincing $L \propto T^4$ tracks give moderate spins, as opposed to extreme Kerr (Davis et al 2006; Shafee et al 2006; Middleton et al 2006; Gou et al 2010). This is as expected from current (probably quite uncertain) supernovae collapse models (see P. Podsiadlowski, these proceedings, also Gammie, Shapiro & McKinney 2004; Kolehmainen & Done 2010) and BHB in low mass X-ray binaries should have a spin distribution which accurately reflects their birth spin. This is because the black hole mass must approximately double in order to significantly change the spin, which is not possible in an LMXB even if the black hole (which must be more than $3 M_{\odot}$) completely accretes the entire low mass ($\lesssim 1 M_{\odot}$) companion star (King & Kolb 1999). However, high spins are derived for two objects which do not have good $L \propto T^4$ tracks, namely GRS1915+105 (McClintock et al 2006, but see Middleton et al 2006) and LMC X-1 (Gou et al 2009)

The high energy tail

However, even the most disc dominated (also termed high/soft state) spectra also have a tail extending out to higher energies with $\Gamma \sim 2$ (see Fig. 1.4a). This tail carries only a very small fraction of the power in the data discussed above, but it can be much stronger and even dominate the energetics. Where the tail coexists with a strong disc component (very high/intermediate or steep power law state) it has $\Gamma > 2$, so the spectra are soft. But where the disc is weak the tail can dominate the total energy, with $\Gamma < 2$ so the spectra are hard (low/hard state), peaking above 100 keV. All these very different spectra are shown in Fig. 1.5a, colour coded in the same way as the long term light-curve (Fig. 1.3). The combination of these two plots shows that typically, hard spectra are only seen at low fractions of Eddington, while disc or disc-plus-soft-tail spectra are seen only at high fractions of Eddington. This is actually very surprising as the classic Shakura-Sunyaev disc is unstable to a radiation pressure instability above $\sim 0.05 L_{Edd}$. Thus we might expect that the disc is disrupted into some other type of flow at high fractions of Eddington, and that we see clean disc spectra only at low fractions of Eddington. This is entirely the reverse of what is seen (as first recognized by Nowak 1995, see also Gierlinski & Done 2004a; DGK07).

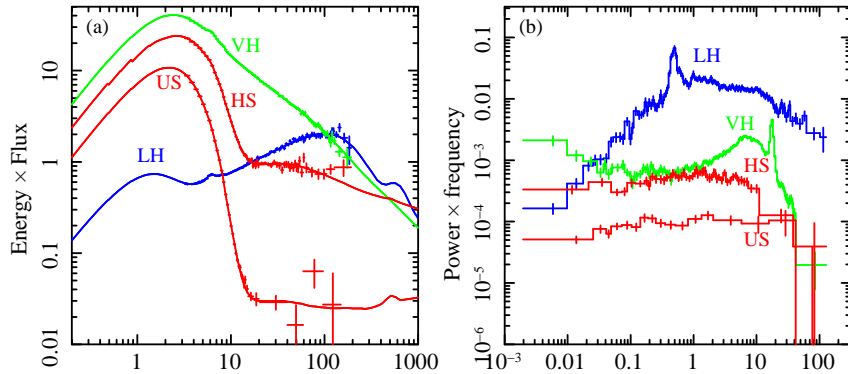


Figure 1.5 a) A selection of spectra from the transient BHB GRO J1655-40. In the electronic version, these different spectral states are colour coded in the same way as the points in the light-curves shown in Fig. 1.3. Soft (US and HS: red) spectra are typically seen at high fractions of Eddington, while hard (LH: blue) spectra are typically seen at low Eddington fractions. Spectra with both strong disc and a strong, soft tail (VH: green) are seen at intermediate luminosities and at the very highest luminosities (DGK07). b) shows the corresponding variability power spectra from 2-60 keV. The variability power on these short timescales drops dramatically when the disc contributes substantially to the spectrum as the disc is very stable on these timescales, so it dilutes the variability of the tail.

The tail has more rapid variability than the disc component (Churazov et al 2001;

Gierlinski & Zdziarski 2005; though the disc variability is enhanced on timescales longer than 1 sec in the low/hard state: Wilkinson & Uttley 2009), typically with large fluctuations on timescales from 100-0.05 seconds. The dynamical (Keplarian orbit) timescale for a $10 M_{\odot}$ black hole at $6R_g$ is 0.005s, so these timescales are at least $10\times$ longer than Keplarian. If the variability is driven by changes in mass accretion rate then the expected timescale is a factor $\alpha(H/R)^2$ longer, so this requires $H/R \sim 1$ i.e. a geometrically thick flow.

1.2.5 Theory of geometrically thick flows: ADAFs

Pressure forces must be important in a geometrically thick flow, by contrast to a Shakura-Sunyaev disc. If these are from gas pressure then the flow must be hot, with protons close to the virial temperature of 10^{12} K. The data require that the electrons are hot in the low/hard state in order to produce the high energy tail via Compton scattering (see section 1.3), but generally only out to 100 keV i.e. 10^9 K. These two very different requirements on the temperature can both be satisfied in a two temperature plasma, where the ion temperature is much hotter than the electron temperature. This happens in plasmas which are not very dense, as the electrons can radiate much more efficiently than the protons, so the electrons lose energy much more rapidly than the protons. Even if the electrons and protons are heated at the same rate then the proton temperature will be hotter than the electrons if the protons and electrons do not interact enough to equilibrate their temperatures. This gives a further requirement that the optical depth of the flow needs to be low.

This leads to the idea of a hot, geometrically thick, optically thin flow replacing the cool, geometrically thin, optically thick Shakura-Sunyaev disc. The exact structure of this flow is not well known at present - Advection Dominated Accretion Flows (ADAFs) are the most well known, but there can also be additional effects from convection, winds and the jet (DGK07). Ultimately, magnetohydrodynamic simulations in full general relativity including radiative cooling are probably needed to fully explore the complex properties of these flows (J. Hawley, this volume).

When ADAFs (Narayan & Yi 1995) were first proposed, a key issue was how to produce such flow from an originally geometrically thin cool disc (to the extent that one theoretician said 'turbulence generated by theorists waving their hands'). However, there is now a mechanism to do this via an evaporation instability. If the cool disc is in thermal contact with the hot flow then there is heat conduction between the two, which can lead to either evaporation of the disc into the hot flow, or condensation of the hot flow onto the disc. At low mass accretion rates, evaporation predominates in the inner disc, giving rise to a radially truncated disc/hot inner flow geometry (Liu et al 1999; Rozanska & Czerny 2000; Mayer & Pringle 2007).

This is exactly the geometry required in the phenomenological truncated disc/hot inner flow models described in the next section

The hot flow can only exist if the electrons and protons do not interact often enough to thermalise their energy. This depends on optical depth, and the flow collapses when $\tau \gtrsim 2 - 3$ which occurs at $\dot{m} = 1.3\alpha^2 \sim 0.01$ for $\alpha = 0.1$ (Esin et al 1997). This is very close to the luminosity of the transition from soft to hard spectra seen on the outburst decline (Maccarone 2003), though more complicated behaviour is seen on the hard to soft transition on the rise (hysteresis: Miyamoto et al 1995; Yu & Yan 2009), plausibly due to the rapid accretion rate changes pushing the system into non-equilibrium states (Gladstone, Done & Gierlinski 2007).

But there are issues. I stress again that the flow should be more complex than an ADAF as these do not include other pieces of physics which are known to be present (convection, winds, the jet, changing advected fraction with radius: see e.g. DGK07). Indeed, standard ADAF solutions are somewhat too optically thin and hot to match the observed Compton spectra (Malzac & Belmont 2009), and this is especially an issue at the lowest L/L_{Edd} where the observed X-ray spectra are far too smooth to be produced by the predicted very optically thin flow (Pszota et al 2008).

1.2.6 Truncated disc/hot inner flow models

These two very different types of solution for the accretion flow can be put together into the truncated disc/hot inner flow model. At high fractions of Eddington we typically see strong evidence for a disc down to the last stable orbit (see Fig. 1.4). At low fractions of Eddington, we can have one of these hot, optically thin geometrically thick flows. The only way to go from one to the other is for the disc to move inwards. As it penetrates further into the flow then more seed photons from the disc are intercepted by the flow so the Compton spectrum softens (see Section 1.3).

The MRI turbulence in the hot inner flow generates the rapid variability at each radius, modulating the mass accretion rate to the next radius. Thus the total variability is the product (not the sum!) of variability from all radii within the hot flow (Lyubarskii 1997; Kotov, Churazov & Gilfanov 2001; Aravelo & Uttley 2006). This rather naturally gives rise to a key observational requirement that the r.m.s. variability σ (see section 1.2.2) in the lightcurve, as measured over a fixed set of frequencies (duration T and sampling Δt), is proportional to the mean intensity I_0 . This is the r.m.s.-flux relation and cannot be produced by a superposition (addition) of uncorrelated events such as the phenomenological 'shot noise' models. Instead this observation *requires* that the fluctuations are multiplicative (Uttley & McHardy 2001; Uttley, McHardy & Vaughan 2005), as sketched in Fig. 1.6.

As the disc extends progressively inwards for softer spectra, the flow at larger

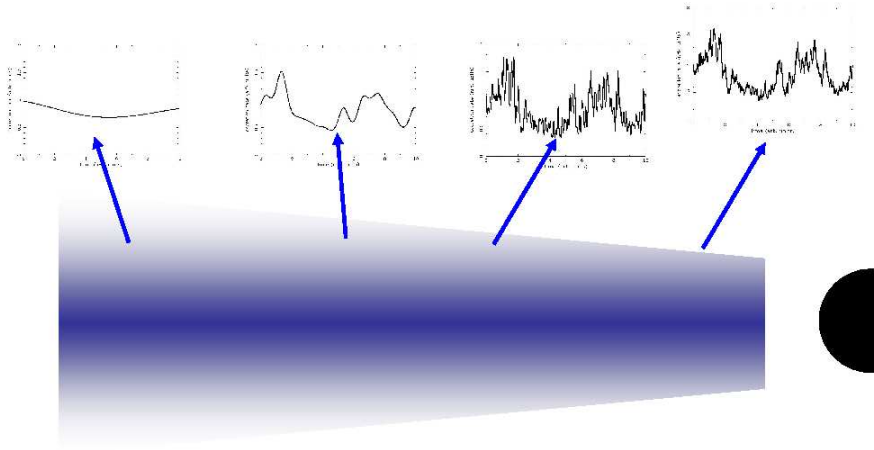


Figure 1.6 A propagating fluctuation model. Large radii produce long timescale fluctuations in mass accretion rate, which modulate faster variations in mass accretion rate produced by fluctuations at smaller radii. Figure courtesy of P. Uttley.

radii cannot fluctuate on such large amplitudes as the disc is underneath it. The large amplitude fluctuations can only be produced from radii inwards of the truncated disc. This gets progressively smaller as the disc comes in, so the longer timescale (lower frequency) fluctuations are progressively lost, so the power spectrum narrows, with ν_b increasing while the amount of high frequency power stays approximately the same, as seen in the data (see Fig. 1.7a). These models can be made quantitative, and can match the major features of the correlated changes in both the energy spectra and the power spectra as the source makes a transition from the low/hard to high/soft states (Fig. 1.7b, Ingram & Done 2010).

However, the power spectrum also contains a characteristic low frequency QPO which also moves along with ν_b (Fig. 1.7a). This can be very successfully modeled in both frequency and spectrum as Lense-Thirring (vertical) precession of the entire hot inner flow (Ingram, Done & Fragile 2009), using the same transition radius as required for the low frequency break in the broad band power spectrum

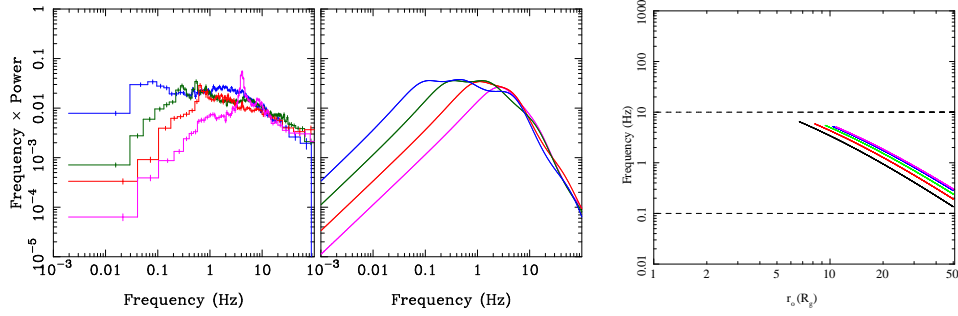


Figure 1.7 a) shows how the power spectra evolve as the source makes a transition from the low/hard to very high state. Low frequency power is progressively lost as the spectrum softens, while the high frequency power remains the same. b) shows how this can be modeled in a truncated disc/hot inner flow geometry, where the transition radius decreases, progressively losing the large radii (low frequency variability) parts of the hot flow (DGK07). The strong low frequency QPO also moves to higher frequencies, consistent with Lense-Thirring precession of the hot flow (Ingram et al 2009).

(Ingram & Done 2010, see Fig. 1.7c). Since this is a model involving vertical precession, the QPO should be strongest for more highly inclined sources, as observed (Schnittman, Homan & Miller 2006).

The hot flow is also a good candidate for the base of the jet, in which case the collapse of the hot flow seen in the high/soft state spectra also triggers the collapse of the jet, as observed (see R. Fender, this volume).

1.2.7 Scale up to AGN

These models can be easily scaled up to AGN, keeping the same geometry as a function of L/L_{Edd} but changing the disc temperature as expected for a super-massive BH. The luminosity scales as M for mass accretion at the same fraction of Eddington, and the inner radius scales as M . Thus the emitting area scales as M^2 so $T^4 \propto L/A \propto 1/M$ so disc temperature *decreases*, peaking in the UV rather than soft X-rays. Interstellar absorption in the host galaxy and in our galaxy effectively screens this emission (see section 1.4.1), so the disc peak cannot be directly observed in the same way as in BHB.

The strong UV flux from the disc also excites multiple UV line transitions (see section 1.4.2) from any material around the nucleus. This environment is much less clean than in LMXRB as there are many more sources of gas to be illumi-

nated in the rich environment of a galaxy centre (molecular clouds, the obscuring torus...), giving strong line emission from the broad line region (BLR) and narrow line region (NLR).

Apart from these differences, we should otherwise see the same behaviour in terms of the spectral and variability changes as the mass accretion rate changes, and in the jet power. Thus these models predict intrinsic changes in the ionizing nuclear spectrum as a function of mass accretion rate as well as changes in the observed spectrum due to obscuration. This is in contrast to the original 'unification models' of AGN in which Seyfert 1 and 2 nuclei were intrinsically the same, but viewed at different orientations to a molecular torus.

There is growing evidence for intrinsic differences in nuclear spectra. The optical emission line ratios can be quite different in *unobscured* AGN of similar mass e.g. LINERS show different line ratios to Seyfert 1s which are different to Narrow Line Seyfert 1s. This is a clear indication that the ionizing spectrum is intrinsically different, as expected from their very different L_{bol}/L_{Edd} . This can be seen directly from compilations of the spectral energy distributions (SED) of these different types of AGN. The fraction of power carried by the X-rays drops for increasing L_{bol}/L_{Edd} in much the same way as for BHB. The soft tail at high L/L_{Edd} carries a smaller fraction of bolometric luminosity so L_x has to be multiplied by a larger factor to get L_{bol} (Vasudevan & Fabian 2007).

The jet should also change with state as in BHB. This gives a clear potential explanation for the origin of radio loud/radio quiet dichotomy. This matches quite well to the observed radio populations (Koerding, Jester & Fender 2006), but there is a persistent suggestion that this is not all that is required, with the most powerful radio jets being found in the most massive AGN (e.g. Dunlop et al 2003). Incorporating super-massive black hole growth and its feedback onto galaxy formation into the semi-analytic codes to model the growth of structures in the Universe may give the answer to this. These show a correlation between super-massive black hole mass and mass accretion rate such that largest black holes in massive ellipticals are now all accreting in gas poor environments so accrete via a hot flow with correspondingly strong radio jet (Fanidakis et al 2010).

1.3 Compton scattering to make the high energy tail

Compton scattering is just an energy exchange process between the photon and electron and the energy exchange is completely analytic. The output photon energy, ϵ_{out} , is given by

$$\epsilon_{out} = \frac{\epsilon_{in}(1 - \beta \cos \theta_{ei})}{1 - \beta \cos \theta_{eo} + (\epsilon_{in}/\gamma)(1 - \cos \theta_{io})}$$

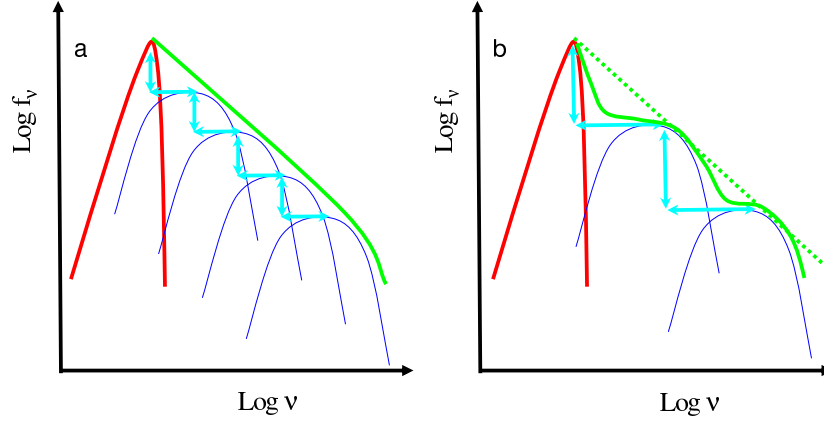


Figure 1.8 a) shows how the spectrum built up from repeated thermal Compton up scattering events for optically thin ($\tau \lesssim 1$) material. A fraction τ of the seed photons (red) are boosted in energy by $1 + 4\Theta$ and then these form the seed photons for the next scattering, so each scattering order (thin lines: blue in electronic version) is shifted down and to the right by the same factor, as indicated by the arrows (cyan), giving a power law (green solid line). b) shows that the same spectral index can be obtained by higher Θ and lower τ but the wider separation of the individual scattering orders result in a bumpy spectrum (green solid line) than a smooth power law (green dotted line).

where θ_{ei} , θ_{eo} and θ_{io} are the angles between the electron and input photon, electron and output photon, and input and output photon, respectively, $\gamma = (1 - \beta^2)^{-1/2}$ is the electron Lorentz factor so that its kinetic energy is $E = (\gamma^2 - 1)^{1/2} m_e c^2$ and $\epsilon = h\nu/m_e c^2$ is the photon energy relative to the rest mass energy of the electron. In general, this simply says whichever of the input electron and photon has the most energy shares some of this with the other.

An electron at rest has $E = 0 < \epsilon$. The photon hits the electron and momentum conservation means that the electron recoils from the collision, so the photon loses energy in Compton downscattering. If the photons and electrons are isotropic and $\epsilon_{in} \ll 1$ then the angle averaged energy loss is $\epsilon_{out} = \epsilon_{in}/(1 + \epsilon_{in}) \approx \epsilon_{in}(1 - \epsilon_{in})$. Thus the change in energy $\epsilon_{out} - \epsilon_{in} = \Delta\epsilon = -\epsilon_{in}^2$. Alternatively, for $\epsilon_{in} \gg 1$ then the photon loses almost all its energy in the collision.

1.3.1 Thermal Compton Upscattering: Theory

Since Comptonization conserves photon number, it is easiest to draw in $\log F(E)$ versus $\log E$ as $F(E)d\log E =$ photon number per bin on a logarithmic energy scale (see section 1.2.1). See also the review by Gilfanov (2010).

In a thermal distribution of electrons, the typical random velocity is set by the electron temperature $\Theta = kT_e/m_e c^2$ as $v^2 \sim 3kT_e/m_e$ so $\beta^2 = 3\Theta$. Again, for isotropic electron and photon distributions this can be averaged over angle to give $\epsilon_{out} = (1 + 4\Theta + 16\Theta^2 + \dots)\epsilon_{in} \approx (1 + 4\Theta)\epsilon_{in}$ for $\Theta \ll 1$. So, in scattering we change energy by $\epsilon_{out} - \epsilon_{in} = \Delta\epsilon = 4\Theta\epsilon_{in}$ and photons are Compton upscattered. Obviously there is a limit to this, since the photon cannot gain more energy than the electron started out with, so this approximation only holds for $\epsilon_{out} \lesssim 3\Theta$.

Photons can only interact with electrons if they collide. The probability a photon will meet an electron can be calculated from the optical depth. An electron has a (Thomson) cross-section σ_T for interaction with a photon. Thus it is probable that the photon will interact if there is one electron within the volume swept out by the photon where the length of the volume is simply the path length, R , and the cross-sectional area is the cross-section for interaction of the photon with an electron, σ_T . Optical depth, τ , is defined as the number of electrons within this volume, so $\tau = nR\sigma_T$ where n is the electron number density. The scattering probability is $e^{-\tau} \approx 1 - \tau$ for $\tau \ll 1$.

The seed photons are initially at some energy, ϵ_{in} , so only a fraction, τ , of these are scattered in optically thin material to energy $\epsilon_{out,1} = (1 + 4\Theta)\epsilon_{in}$. But these scattered photons themselves also can be scattered to $\epsilon_{out,2} = (1 + 4\Theta)\epsilon_{out,1} = (1 + 4\Theta)^2\epsilon_{in}$. These photons can be scattered again to $\epsilon_{out,3}$ etc until they reach the limit of the electron energy after N scatterings where $\epsilon_{out,N} = (1 + 4\Theta)^N \epsilon_{in} \sim 3\Theta$. Since the energy boost and fraction of photons scattered is constant then this gives a power law of slope $\log f(\epsilon) \propto \ln(1/\tau)/\ln(1 + 4\Theta)$ i.e. $f(\epsilon) \propto \epsilon^{-\alpha}$ with $\alpha = \ln \tau / \ln(1 + 4\Theta)$. This is a power law from the seed photon energy at ϵ_{in} up to 3Θ . Thus the power law index is determined by *both* the temperature and optical depth of the electrons. These cannot be determined independently without observations at high energy to constrain Θ as the same spectral index could be produced by making τ smaller while increasing Θ (see Fig. 1.8a and b). However, there are some constraints as the spectrum is only a smooth power law in the limit where the orders overlap i.e. τ not too small and Θ not too big and the energy bandpass is not close to either the electron temperature or seed photon energy (see Fig. 1.8a and b).

This list of caveats means that often a power law is *not* a good approximation for a Comptonized spectrum. If the temperatures are non-relativistic and the optical depth not too small then COMPTT (Titarchuk 1994) or NTHCOMP (Zdziarski

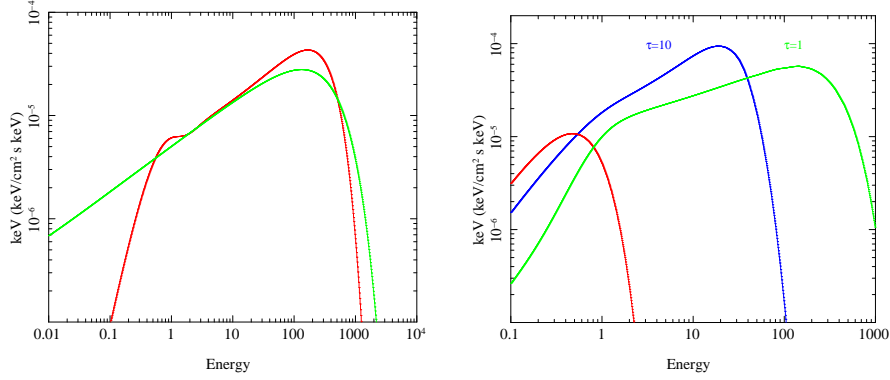


Figure 1.9 a) The dark grey (red) line shows the thermal Comptonization spectrum computed by COMPPS for $\tau = 2$ and $kT_e = 100$ keV with seed photons at 0.2 keV (using $\text{geom}=0$ and covering fraction=1). The slight bump at the seed photon energy is from the fraction $\exp(-\tau)$ of the seed photons which escape without scattering. The Compton upscattered spectrum does not extend down below the seed photon energy, so there is an abrupt downturn below $3kT_{seed} = 0.6$ keV. By contrast, an exponentially cutoff power law spectrum (light grey/green) has a much more gradual rollover at the electron temperature, and extends below the seed photons. These two differences can mean that an exponentially cutoff power law is a poor approximation to a Comptonised spectrum. b) shows an energetic approach to Comptonisation for $\ell_h/\ell_s = 10$ with $\tau = 10$ (dark grey/blue) and 1 (light grey/green). Each of these two Comptonised spectra contains $10\times$ more energy than the seed photons (thermal spectrum at low energies: red), but have different spectral index and electron temperature.

Johnson & Magdziarz 1996, where the 'n' in front of thcomp denotes that it does not have the reflected component of Zycki, Done & Smith 1999) can be used as these both include the downturn in the Compton emission close to the seed photon energy which affects the derived disc properties (Kubota & Done 2004), as well as the rollover at the electron temperature.

However, for temperatures much above ~ 100 keV with good high energy data then relativistic corrections become important and COMPPS (Poutanen & Svensson 1996) or EQPAIR (Coppi 1999) should be used. The Compton rollover at the electron temperature is rather sharper than an exponential, so using an exponentially cutoff power law is not a good approximation (see Fig. 1.9a), and will distort the derived reflected fraction (see Section 1.5).

In optically thick Comptonization, with $\tau \gg 1$, almost all the photons are scattered each time so almost all of them end up at the electron temperature of 3Θ forming a Wien peak (Fig. 1.10a). The average distance a photon travels before scattering is $\tau = 1$ i.e. a mean free path of $\lambda = 1/(n\sigma_T)$. Thus after 1 scattering, the distance travelled is $d_1^2 = \lambda^2 + \lambda^2 - 2\lambda^2 \cos \theta_{12}$ while after 2

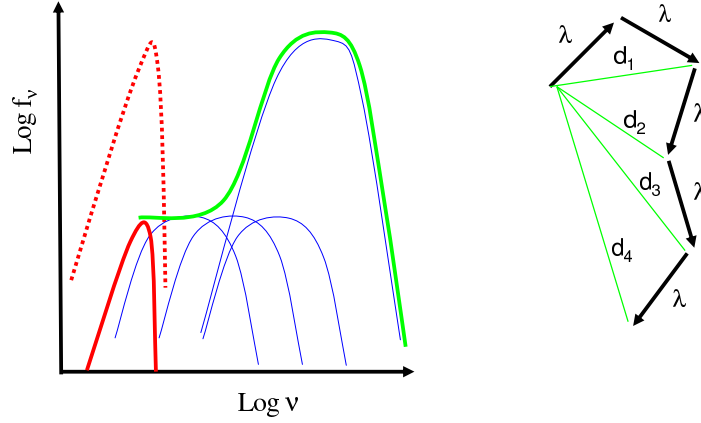


Figure 1.10 The left hand panel shows how the spectrum built up from repeated thermal Compton up scattering events for optically thick ($\tau \gtrsim 1$) material. Almost all ($\exp^{-\tau}$) the original seed photons (red dotted line) are scattered multiple times until they all pile up at the mean electron energy of $\sim 3\Theta$. The right hand sketch shows the electron path, randomising direction by scattering after an average distance $\lambda = 1/n\sigma_T$ (i.e. travelling $\tau = 1$).

scatterings this is $d_2^2 = d_1^2 + \lambda^2 - 2\lambda d_1 \cos \theta_{2,3}$ and after N scatterings $d_N^2 = d_{N-1}^2 + \lambda^2 - 2\lambda d_{N-1} \cos \theta_{N,N+1}$. Since the scattering randomizes the direction then the angles average out, leaving $d_N^2 = N\lambda^2 = N/(n\sigma_T)^2$. The photon can escape when $d_N = R$, so the average number of scatterings before escape is $N \sim \tau^2$ (see Fig. 1.10b).

The amount of energy exchange from the electrons to photons in Comptonization can be roughly characterized by the Compton y parameter. The fractional change in energy of the photon distribution, y , is the average number of scatterings times average fractional energy boost per scattering such that $y \approx (4\Theta + 16\Theta^2)(\tau + \tau^2) \approx 4\Theta\tau^2$ in the optically thick, low temperature limit. If $y \ll 1$ then the electrons make very little difference to the spectrum, while for $y \gtrsim 1$, Comptonization is very important in determining the emergent spectrum.

1.3.2 Comptonization via energetics

Describing the spectrum in terms of τ and Θ is the 'classical' way to talk about Compton scattering. But the physical situation is better described by τ and energetics. There is some electron region with optical depth τ , heated by a power input ℓ_h , making a Comptonized spectrum from some seed photon luminosity ℓ_s . Now

we are doing this by luminosity instead of photon number we should plot $\nu F(\nu)$ rather than $F(\nu)$. The seed photons peak at $\sim 3kT_{seed}$, with $\nu F(\nu) = \ell_s$. The 'power law' Compton spectrum always points back to this point, forming a power law of energy index $\alpha \sim \log \tau / \log(1 + 4\Theta)$ which extends from here to $\sim 3kT_e$, and has total power ℓ_h . The resulting equation can then be solved for Θ (see Haardt & Maraschi 1993). This is shown in Fig. 1.9b, using the EQPAIR model. The seed photons (red) are Comptonised by hot electrons which have $10\times$ as much power as in the seed photons. For a large optical depth (blue: $\tau = 10$) this energy is shared between many particles, so the electron temperature is lower than for a smaller optical depth (green: $\tau = 1$). The spectrum cannot extend out to high energies, so has to be harder in order to contain the requisite amount of power.

This energetic approach gives more physical insight when we come to consider seed photons produced by reprocessing of the hard X-ray photons illuminating the disc (see section 1.6.2).

1.3.3 Thermal Compton Scattering: Observations of Low/Hard State

Fig. 1.11 shows two examples of low/hard state spectra from a BHB, one which rolls over at ~ 90 keV, and one which extends to ~ 200 keV. Both rollovers look like thermal Comptonization, but with different temperatures (~ 30 keV, and ~ 100 keV, respectively, i.e. $\Theta \sim 0.06$ and 0.2). The optical depth can then be derived from the spectral index but not quite as easily as described above as τ is of order unity rather than $\ll 1$ as required for the analytic expression. A more proper treatment gives $\tau \sim 0.6$. Then the fraction of unscattered seed photons should be only $1 - e^{-\tau}$ but we actually see more than this in Fig. 1.11a. Thus we require that not all the seed photons go through the hot electron region i.e. the geometry is either a truncated disc or the electron regions are small compared to the disc - either localised magnetic reconnection regions above the disc or a jet. See Section 1.6.2 for how the energetics of Compton scattering strongly favour the truncated disc.

The spectra shown above are fit assuming that the observed soft X-ray component provides the seed photons for the Compton upscattering. This can be seen explicitly where there are multiwavelength observations, extending the bandpass down to the optical/UV where the outer parts of the disc can dominate the emission. Fig. 1.11a shows this for a bright low/hard state in the transient BHB XTE J1753.5-0127 (Chiang et al 2009). It is clear that extrapolating the hard X-ray power law down to the optical/UV will produce far more emission than observed. Thus the hard X-ray power law must break between the UV and soft X-ray, i.e. the seed photons for the Compton upscattering should be somewhere in this range. Since there is an obvious soft X-ray thermal component, this is the obvious seed photon identification. Fitting the soft X-rays with a disc component slightly underproduces

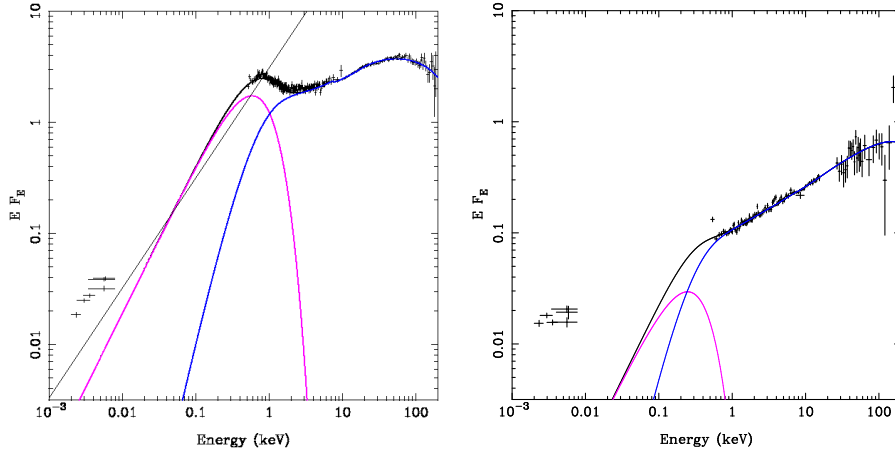


Figure 1.11 The unabsorbed data from the BHB transient 1753.5-0127 modelled with a disk (thermal component peaking at 0.6 keV: magenta) and thermal Compton scattering of seed photons from the disk (peaking at 80 keV: blue). The left hand panel shows a bright low/hard state, where the optical/UV data clearly lie far below the extrapolated hard X-ray emission, indicating that the X-ray spectrum must break (i.e. have its seed photons) somewhere between the UV and soft X-ray bandpass. The disk is then the obvious source for these seed photons. The optical/UV points are some way below the extrapolated disc emission, but this leaves room for hard X-ray reprocessing, and possibly some component from the radio jet spectrum extrapolated up to this band (thin black line). However, the right panel shows the very different dim low/hard state spectrum from the same source. There is still a very weak soft X-ray component, but the optical/UV now lie on the extrapolated hard X-ray spectrum, making it more likely that the seed photons for the Compton scattering are at energies below the optical, i.e. are probably cyclo-synchrotron (Chiang et al 2009)

the optical/UV emission, but this can be enhanced by reprocessing of hard X-rays illuminating the outer disc (van Paradijs 1996).

However, for dimmer low/hard states, the hard X-rays extrapolate directly onto the optical/UV emission (Fig. 1.11b: Chiang et al 2009; Motch et al 1985). This looks much more like the seed photons are at lower energies than the optical. In the truncated disc picture, the disc can be so far away that it subtends a very small solid angle to the hot electron region which is concentrated at small radii. Thus the amount of seed photons from the disc illuminating the hot electrons can be very small, and can be less important than seed photons produced by the hot flow itself. The same thermal electrons as make the Compton spectrum can make both bremsstrahlung (from interactions with protons) and cyclo-synchrotron (from interactions with any magnetic field such as the tangled field produced by the MRI). The bremsstrahlung spectrum will peak at kT_e , so these seed photons have similar

energies to the electrons so cannot gain much from Compton scattering. However, the cyclo-synchrotron typically peak in the IR/optical region so these can be the seed photons for a power law which extends from the optical to the hard X-ray region (Narayan & Yi 1995; Di Matteo, Celotti & Fabian 1997; Wardzinski & Zdziarski 2000; Malzac & Belmont 2009).

Evidence for a change in seed photons is also seen in the variability (see R. Hynes, this volume). In bright states (both bright low/hard and high/soft/very high states) the optical variability is a lagged and smoothed version of the X-ray variability, showing that it is from reprocessed hard X-ray illumination of the outer accretion disc. However, this changes in the dim low/hard state, with the optical having more rapid variability than the hard X-rays, and often *leading* the hard X-ray variability (Kanbach et al 2001; Gandhi et al 2008; Durant et al 2008; Hynes et al 2009). This completely rules out a reprocessing origin, clearly showing the change in the optical emission mechanism.

1.3.4 Non-Thermal Compton Scattering: High/Soft State

While the low/hard state can be fairly well described by thermal Compton scattering, the same is not true for the tail seen in the high soft state. This has $\Gamma \sim 2$ and clearly extends out past 1 MeV, and probably past 10 MeV for Cyg X-1 (Gierlinski et al 1999; McConnell et al 2002), as shown in Fig. 1.12a. If this were thermal Compton scattering then the electron temperature must be $\Theta \gtrsim 1$, requiring optical depth $\tau \ll 1$ in order to produce this photon index. The separate Compton orders are then well separated and the spectrum should be bumpy (see Fig. 1.8b) rather than the smooth power law seen in the data (the bump in the data is from reflection: see Section 1.5). Thus this tail cannot be produced by thermal Comptonization.

Instead it can be non-thermal Compton scattering, where the electron number density has a power law distribution rather than a Maxwellian i.e. $n(\gamma) \propto \gamma^{-p}$ from $\gamma = 1$ to γ_{max} . Going back to the original equation for the Compton scattered energy boost, for $\gamma \gg 1$ the output photon is beamed into a cone of angle $1/\gamma$ along the input electron direction. This gives an angle averaged output photon energy of $\epsilon_{out} = (4/3\gamma^2 - 1)\epsilon_{in} \approx \gamma^2\epsilon_{in}$ for an isotropic distribution of input photons and electrons. Thus the Compton scattered spectrum extends from ϵ_{in} to $\gamma_{max}^2\epsilon_{in}$, forming a power law from a single scattering order.

The power law index of the resulting photon spectrum can be calculated from an energetic argument. The rate at which the electrons lose energy is the rate at which the photons gain energy, giving $F(\epsilon)d\epsilon \propto \dot{\gamma}n(\gamma)d\gamma$ where $\dot{\gamma} \propto \gamma^2$ is the rate at which a single electron of energy γ loses energy and $n(\gamma)$ is the number of electrons at that energy. Thus $F(\epsilon) \propto \gamma^2\gamma^{-p}d\gamma/d\epsilon$. Since $\epsilon \sim \gamma^2\epsilon_i$ then $d\epsilon/d\gamma =$

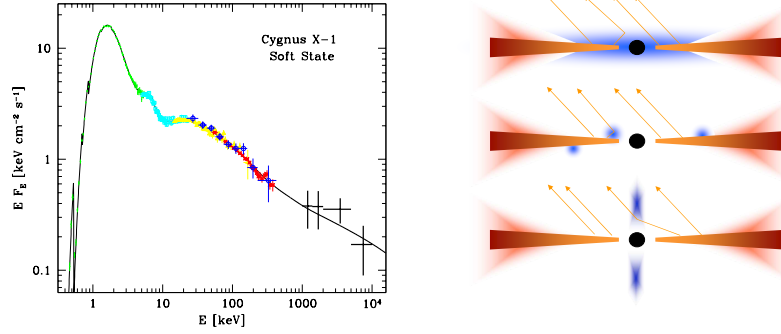


Figure 1.12 The left panel shows a composite spectrum of the high/soft state of Cyg X-1 from multiple instruments. Interstellar absorption is not removed, causing the drop below 1 keV. Nonetheless, the disc clearly dominates the low energy data (BeppoSAX LECS: green) while the soft tail extends out to ~ 10 MeV (OSSE COMPTEL: black). The tail itself is smooth, but there is curvature and spectral features seen from 5-20 keV (BeppoSAX HPGSPC: cyan) from reflection (see Section 1.5). Figure from McConnell et al (2002). The right panel shows the potential source geometries in which the disc photons can dominate the spectrum at low energies as observed. This requires that either the electron acceleration region is optically thin, or that it is localized, perhaps as active regions over the disc or in the (base of the) jet.

2γ so $F(\epsilon) \propto \gamma^{-(p-1)} \propto \epsilon^{-(p-1)/2}$ i.e. an energy spectral index of $\alpha = (p-1)/2$ (G. Ghisellini, private communication).

For an optically thin electron region, the electrons intercept only a fraction τ of the seed photons, and scatter them to $\gamma_{max}^2 \epsilon_{in}$ with an energy spectral index of $(p-1)/2$. These can themselves be scattered into a second order Compton spectrum to $\gamma_{max}^2 (\gamma^2 \epsilon_{in}) = \gamma^4 \epsilon_{in}$ but very soon the large energy boost means that these hit the limit of the electron energy of $\epsilon_{out} = \gamma_{max}$. The resulting spectrum is shown schematically in Fig. 1.13.

Thus the high/soft state of Cyg X-1 requires $\gamma_{max} > 30$ to get seed photons from the disc at 1 keV upscattered to 1 MeV, or $\gamma_{max} > 100$ to get to 10 MeV, while the energy spectral index of $1.2 = (p-1)/2$ implies $p \sim 3$. Such non-thermal Compton spectra can be modelled using either COMPPS or EQPAIR.

Fig. 1.12a shows that the seed photons from the disc are clearly seen as distinct from the tail. This requires that either the optical depth is very low, or the electron acceleration region does not intercept many of the seed photons from the disc i.e. localized acceleration regions as shown schematically in Fig. 1.12b.

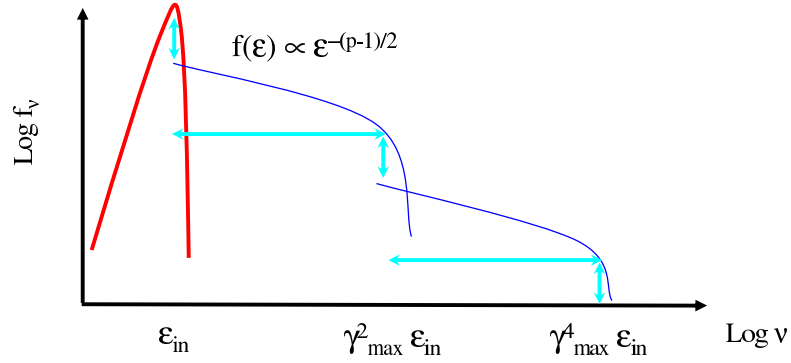


Figure 1.13 Schematic of non-thermal Compton scattering, where the seed photons (red) form a power law from a single scattering due to the power law electron distribution from $\gamma = 1 - \gamma_{max}$.

1.3.5 Thermal - Nonthermal (Hybrid) Compton Scattering

The high/soft states can transition smoothly into the very high or intermediate state spectra, with the tail becoming softer and carrying a larger fraction of the total power (Fig. 1.14a). The disc then merges smoothly into the tail, showing that the hot electron region completely covers the inner disc emission and it is optically thick. The tail still extends up to 1 MeV, so clearly also contains non-thermal electrons, and is rather soft but has a complex curvature (see Fig. 1.14b).

The extent of the tail shows that there must be non-thermal Compton scattering, as in the high/soft state. However, the tail is softer so the electron index must be more negative than in the high/soft state spectrum, so the mean electron energy is lower. Yet the lack of direct disc emission requires an optical depth of $\gtrsim 1$. This means that there are multiple Compton scattering orders forming the spectrum in a similar way to thermal Compton scattering, but from a non-thermal distribution. The energetic limit to which photons can be scattered is γ_{max} but because the energy boost on each scattering is small, the spectrum actually rolls over at $m_e c^2 = 511$ keV as the cross-section for scattering drops at this point where $\gamma\epsilon \sim 1$ (as the cross-section transitions to Klein-Nishina rather than the constant Thomson cross-section seen at lower collision energies). Thus optically thick, nonthermal Comptonized spectra with a steep power law electron distribution does not produce a power law spectrum. Instead there is a break at 511 keV (Ghisellini 1989), as shown schematically in Fig. 1.15a, which means that this cannot fit the observed

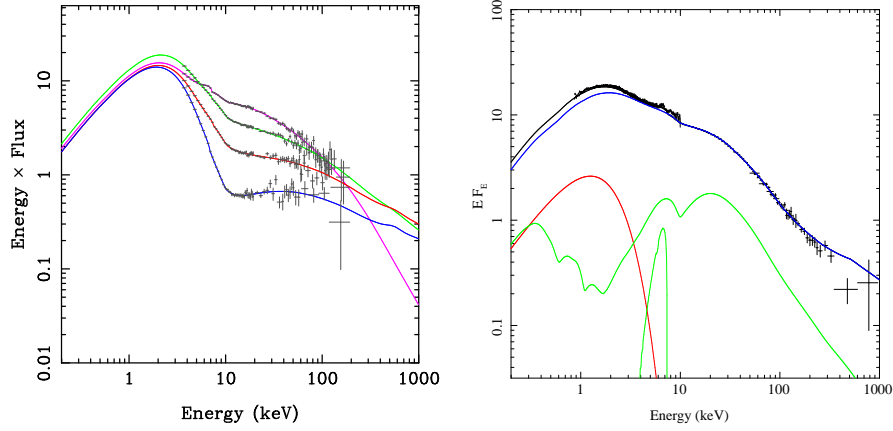


Figure 1.14 a) Transition from high/soft to extreme very high state in the BHB transient XTE J1550-564. b) Broader band spectrum of the extreme very high state. The emission is dominated at all energies by the Comptonized continuum, and there is very little of the disc emission (thermal component peaking at ~ 1 keV: red) that can be seen directly. This requires that the corona is optically thick and covers most of the inner disc, in contrast to the possible high/soft state geometries. The reflected continuum and its associated iron emission line (light grey/green) are also shown (see section 1.5).

tail at high energies seen in the very high state spectrum, as shown in Fig. 1.15b (Gierlinski & Done 2003)

Thus neither thermal nor non-thermal Compton scattering can produce the tail seen in these very high state data. Instead, the spectra require both thermal and non-thermal electrons to be present. This could be produced in a single acceleration region, where the initial acceleration process makes a non-thermal distribution but where the resulting electrons have a hybrid distribution due to lower energy electrons predominantly cooling through Coulomb collisions (which thermalize) while the higher energy electrons maintain a power law shape by cooling via Compton scattering (Coppi 1999). Such hybrid thermal/non-thermal spectra can be modeled in XSPEC using either COMPPS or EQPAIR. Alternatively, this could indicate that there are two separate acceleration regions, one with thermal electrons, perhaps the remnant of the hot inner flow, and one with non-thermal, perhaps magnetic reconnection regions above the disc or the jet (DGK07). This could be modeled by two separate COMPPS or EQPAIR components, one of which is set to be thermal, and the other set to be non-thermal.

Whatever the electrons are doing, they are optically thick and cover the inner disc. Hence it is very difficult to reconstruct the intrinsic disc spectrum in these states. The derived temperature and luminosity of the disc depend on how the tail

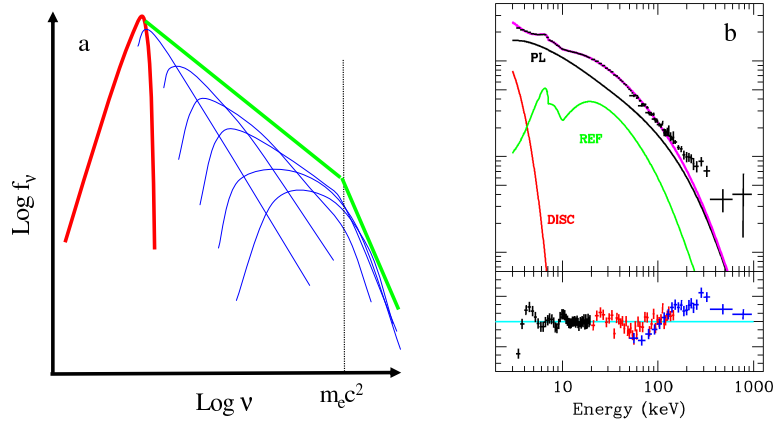


Figure 1.15 a) Spectrum resulting from a steep power law electron distribution which is optically thick ($\tau \gtrsim 1$ rather than $\tau \gg 1$). The steep power law means that the mean electron energy is low, so the spectrum is built up from multiple Compton scatterings in a way similar to thermal Comptonization. Thus $\epsilon\gamma \sim 1$ at $\epsilon \sim 1$ i.e. at 511 keV, so the spectrum breaks due to the reduction in cross-section. b) shows how this means that such a steep power law electron distribution cannot fit the high energy tail seen in the very high state.

is modeled. A simple power law model for the tail means that it extends below the putative seed photons from the disc. Instead, in Compton upscattering, the continuum rolls over at the seed photon energy, so there are fewer photons at low energies from the tail so the disc has to be more luminous and/or hotter in order to match the data. Compton scattering conserves photon number, so all the photons in the tail were initially part of the disc emission, so the intrinsic disc emission is brighter than that observed by this (geometry dependent) factor. This means that the intrinsic disc luminosity and temperature cannot be unambiguously recovered from the data when $\tau \gtrsim 1$, where the majority of photons from the disc are scattered into the tail (Kubota et al 2001; Kubota & Done 2004; Done & Kubota 2006; Steiner et al 2009).

For more observational details of spectral states see Remillard & McClintock (2006) and Belloni (2009).

1.4 Atomic Absorption

The intrinsic continuum is modified by absorption by material along the line of sight. This can be the interstellar medium in our galaxy the host galaxy of the X-ray source, or material associated with the source. For AGN this can be the molecular torus, the NLR or BLR clouds, or an accretion disc wind. For BHB this is just an accretion disc wind, and any wind from the companion star. For magnetically truncated accretion discs such as seen in the intermediate polars (white dwarf) and accretion powered millisecond pulsars (neutron stars) there is an accretion curtain which can be in the line of sight (de Martino et al 2004), while for extreme magnetic fields the disc is completely truncated and there is only an accretion column (polars in white dwarfs) but this overlays the X-ray hot shock, giving complex absorption (Done & Magdziarz 1998).

Again the key concept is optical depth, $\tau = \sigma(E)nR$, only now the cross-section, $\sigma(E)$, has a complex dependence on energy (rather than the constant electron scattering cross-section, σ_T , for energies below 511 keV). We can combine $nR = N_H$ as the number of Hydrogen atoms along a line of sight volume with cross-sectional area of 1 cm^{-2} , so the optical depth is simply related to column density by $\tau(E) = \sigma(E)N_H$.

1.4.1 Neutral Absorption

The photo-electric absorption cross-section of neutral hydrogen is zero below the threshold energy of 13.6 eV, below which the photons do not have enough energy to eject the electron from the atom. It peaks at this threshold edge energy at a value of $6 \times 10^{-18} \text{ cm}^{-2}$ and then declines as $\approx (E/E_{\text{edge}})^{-3}$. Thus the optical depth is unity for a Hydrogen column of $1.6 \times 10^{17} \text{ cm}^{-2}$ at 13.6 eV while a typical column through our galaxy is $> 10^{20} \text{ cm}^{-2}$, showing how effectively the UV emission is attenuated.

The drop in cross-section with energy means that an H column of 10^{20} cm^{-2} has $\tau = 1$ at an energy of $\sim 0.2 \text{ keV}$, allowing the soft X-rays to be observed. Fig. 1.16a shows how a hydrogen column of $\log N_H = 19, 20, 21, 22, 23$ progressively absorbs higher energy X-rays. However, the column is not made up solely of H. There are other, heavier, elements as well. These have more bound electrons, but the highest edge energy will be from the inner $n = 1$ shell (also termed the K shell) electrons as these are the closest to the nuclear charge. Since this charge is higher, then the $n = 1$ electrons are more tightly bound than those of H e.g. for He it is 0.024 keV, C, N, O is 0.28, 0.40 and 0.53 keV. These elements are less abundant than H so they form small increases in the total cross-section. Fe is the last astrophysically abundant element, and this has a K edge energy of 7.1 keV.

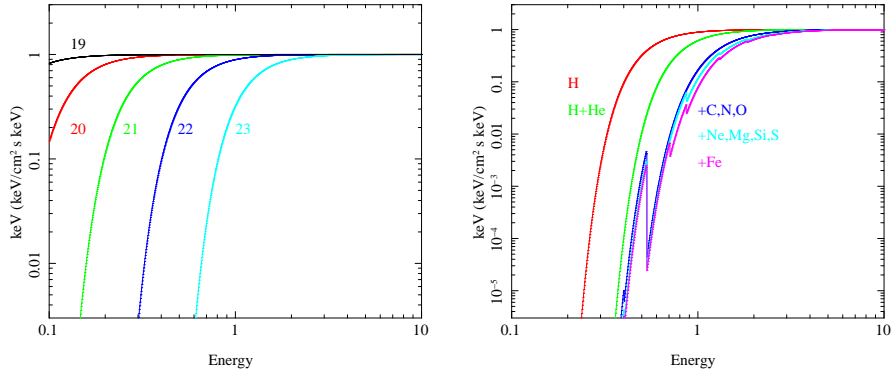


Figure 1.16 a) Photo-electric absorption from Hydrogen alone, in a column of $\log N_H = 19, 20, 21, 22, 23$ (from left to right). b) shows how the absorption for a column of $\log N_H = 22$ changes as progressively heavier atomic numbers are added.

Fig. 1.16b shows this for column of 10^{22} cm^{-2} for progressively adding higher atomic number elements assuming solar abundances. Helium has an impact on the total cross-section, but additional edges from heavier elements are important contributions to the total X-ray absorption, especially Oxygen.

In XSPEC, this can be modeled using TBABS/ZTHABS (Wilms, Allen and McCray 2000, where the latter has redshift as a free parameter) or PHABS/ZPHABS (Balucinska-Church & McCammon 1992) if the abundances are assumed to be solar, or TBVARABS/ZVPHABS if the data are good enough for the individual element abundances to be constrained via their edges such as in GRS 1915+104 (Lee et al 2002). However, with excellent spectral resolution data from gratings then the line absorption (especially from neutral Oxygen) becomes important (see section 1.4.3), and TBNEW (see J. Wilms web page at <http://pulsar.sternwarte.uni-erlangen.de/wilms/research/tbnew>) should be used (Juett, Schulz & Chakrabarty 2004).

1.4.2 Ionised Absorption

Photo-electric absorption leaves an ion i.e. the nuclear charge is not balanced. Thus all the remaining electrons are slightly more tightly bound, so all the energy levels increase. The ion can recombine with any free electrons, but if the X-ray irradiation is intense then the ion can meet an X-ray photon before it recombines, so that the absorption is dominated by photo-ionized ions. For H, this means there is no photo-electric absorption, since it has no bound electrons after an ionization event, so some fraction of the total cross-section disappears. Helium may then have 1 electron left, so its edge moves to 0.052 keV. At higher ionizations, Helium is completely ionized, so its contribution to the total cross-section is lost and there

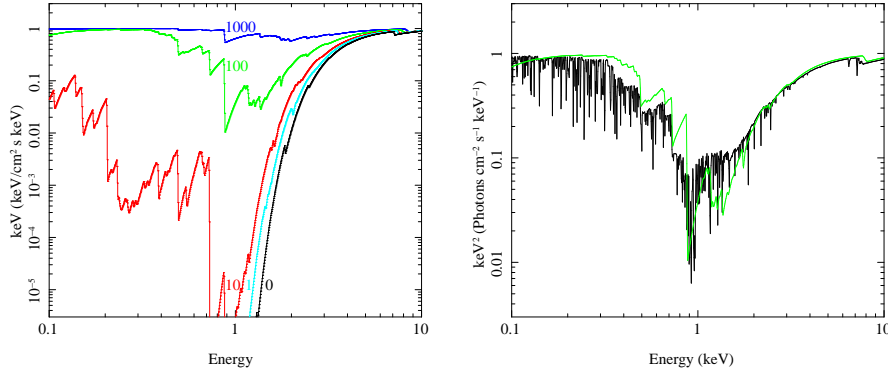
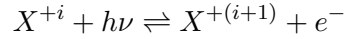


Figure 1.17 a) The photo-electric (bound-free) absorption of a column of $N_H = 10^{23} \text{ cm}^{-2}$ and ionization state increasing progressively from bottom to top with $\xi = 0$ (black), 1 (cyan), 10 (red), 100 (green) and 1000 (blue) for photo-ionization by a power law of $\Gamma = 2$ as calculated by ABSORI. b) shows how the opacity of partially ionized material ($\xi = 100$) can instead be dominated by bound-bound (line) transitions using a proper photo-ionisation code such as XSTAR.

are only edges from (ionized) C, N, O and higher atomic number elements. Thus the effect of going to higher ionization states is to reduce the overall cross-section as the numbers of bound electrons are lower. In the limit where all the elements are completely ionized, there is no photo-electric absorption at all.

The ion populations are determined by the balance between photo-ionization and electron recombination. For a given element X , the ratio between X^{+i} and the next ion stage up, $X^{+(i+1)}$ is given by the equilibrium reaction



The photo-ionization rate depends on the number density of the ion N_X^{+i} and of the number density of photons, n_γ , above the threshold energy ν_{edge} for ionization for that species. This number density can be approximated by $n_\gamma \sim L/(h\nu 4\pi r^2 c)$ where L is the source luminosity, $h\nu$ is the typical photon energy and $4\pi r^2 c$ is the volume swept out by the photons in 1 second. Actually, what really matters is the number of photons past the threshold energy which photo-ionize the ion, so this depends on spectral shape as well.

Equilibrium is where the photo-ionization rate, $N_X^{+i} n_\gamma \sigma(X^{+i}) c$ balances the recombination rate $N_X^{+(i+1)} n_e \alpha(X^{+(i+1)}, T)$ where $\sigma(X^{+i})$ is the photoelectric absorption cross-section for X^{+i} and $\alpha(X^{+(i+1)}, T)$ is the recombination coefficient for ion $X^{+(i+1)}$ at temperature T . Hence the ratio of the abundance of the ion

to the next stage down is given by

$$\frac{N_X^{+(i+1)}}{N_X^{+i}} = \frac{n_\gamma \sigma(X^{+i}) c}{n_e \alpha(X^{+(i+1)}, T)} \propto \frac{n_\gamma}{n_e}$$

Thus the ratio of photon density to electron density determines the ion state. If the photon density is highest, the ion meets a photon first, so is ionized to the next stage. Conversely, if the electron density is higher, then the ion meets an electron first and recombines to the lower ion stage. The ratio of photon to electron number density can be written as $n_\gamma/n_e = \xi/(4\pi h\nu c)$ where $\xi = L/nr^2$ is the photo-ionization parameter. There are other ways to define this such as $\Xi = P_{rad}/P_{gas} = L/(4\pi r^2 c n_e kT) = \xi/(4\pi c kT)$ but whichever description is used, the higher the ionization parameter, the higher the typical ionization state of each element.

In general, the equilibrium reaction means that there are at least two fairly abundant ionization stages for each element, so as long as the higher ionization stage is not completely ionized then there are multiple edges from each element as each higher ion stage has a higher edge energy as the electrons are more tightly bound. This can be clearly seen in Fig. 1.17a, where the H-like Oxygen (O^{+7}) edge at 0.87 keV is accompanied by the He-like (O^{+6}) edge at 0.76 keV for $\xi = 100$ and 10.

The ABSORI (Done et al 1992) model in XSPEC calculates the ion balance for a given (rather than self-consistently computed) temperature and hence gives the photo-electric absorption opacity from the edges. However, this can be very misleading as it neglects line opacities (see below, and Fig. 1.17b)

1.4.3 Absorption Lines

There are also line (bound-bound) transitions as well as edges (bound-free transitions). These can occur whenever the higher shells are not completely full. Hence Oxygen can show absorption at the n=1 to n=2 (1s to 2p) shell transition even in neutral material whereas elements higher than Ne need to be ionized before this transition can occur. The cross-section in the line depends on the line width. This is described by a Voigt profile. The 'natural' line width is set by the Heisenburg uncertainty relation between the lifetime of the transition $\Delta t \Delta \nu \lesssim \hbar$. This forms a Lorentzian profile, with broad wings. However, the ions also have some velocity due to the temperature of the material $v_{thermal}^2 \sim kT_{ion}/m_{ion}$. Any additional velocity structure such as turbulence adds in quadrature so $v^2 = v_{thermal}^2 + v_{turb}^2$. These velocities Doppler shift the transition, giving a Gaussian core to the line. This combination of Gaussian core, with Lorentzian wings, is termed a Voigt profile (see Fig. 1.18a)

The line equivalent width is the width of a rectangular notch (down to zero) in

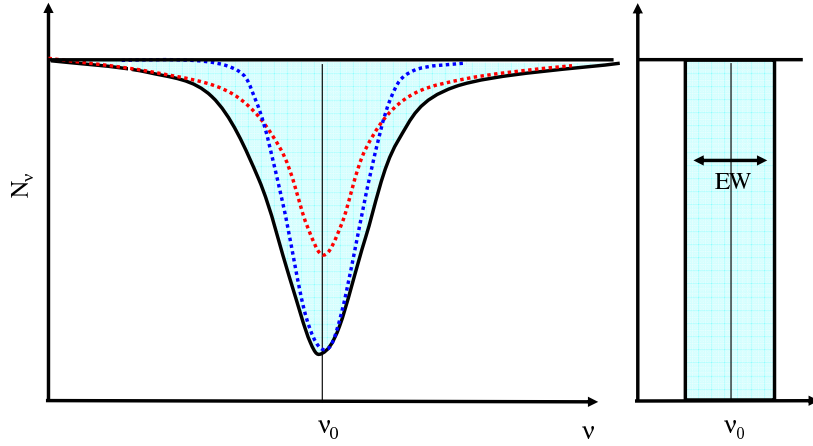


Figure 1.18 a) The Voigt profile of an absorption line (black line), with a Doppler core (dark grey/blue dotted line) and Lorentzian wings (light grey/red dotted line). b) The equivalent width of an absorption line is the width of a rectangular notch in the spectrum at the rest wavelength which contains the same number of photons as in the line.

the spectrum which contains the same number of photons as in the line profile, as shown in Fig. 1.18b. The equivalent width of the line grows linearly with the column density of the ion when the line is optically thin in its core, as the line gets deeper linearly with column (called unsaturated). However, this linear behaviour stops when the core of the line becomes optically thick i.e. none of the photons at the line core can escape at the rest energy of the transition. Increasing the column cannot lead to much more absorption as there are no more photons at the line center to remove. The wings of the line can become optically thick but Doppler wings are very steep so the line equivalent width does not increase much as the column increases (called saturated). Eventually, the Lorentzian wings start to become important, and then the line equivalent width increases as the square root of the column density (called heavily saturated). This relation between column and line equivalent width is termed a 'curve of growth'. While the linear section of this is unique, the point at which the line becomes saturated depends on the Doppler width of the line, i.e. on the velocity structure of the material as shown in Fig. 1.19.

For 'reasonable' velocities, the line absorption equivalent width can be larger than the equivalent width of the edges, so that line transitions dominate the absorption spectrum. Fig 1.17b shows the total absorption (line plus edges computed using WARMABS, a model based on the XSTAR photo-ionization code (Kallman & Bautista 2001; Kallman et al 2004) compared to the more approximate ionization code which just used edge opacities (ABSORI in XSPEC). The differences are

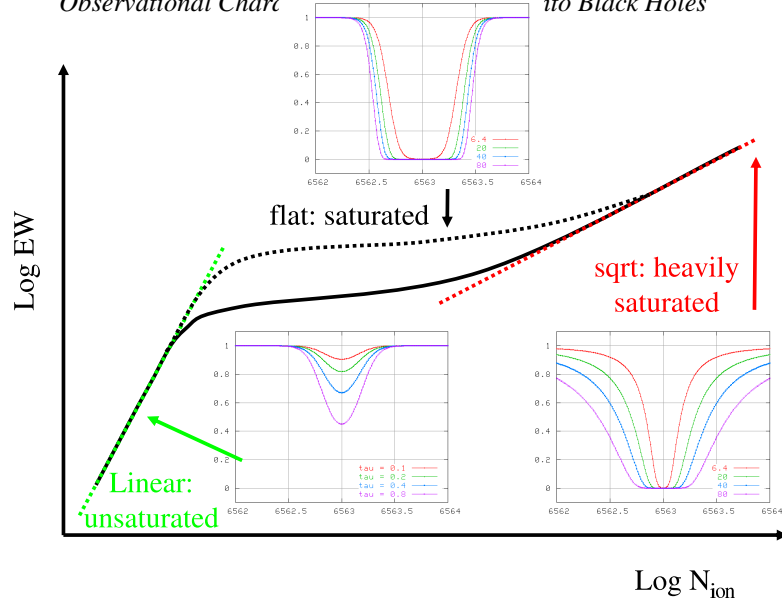


Figure 1.19 A curve of growth. On the unsaturated section the line equivalent width increases linearly with increasing column. However, once the line becomes optically thick in the core, increasing the column does not lead to an increase in absorption as the line center is black. The Doppler wings are very steep so there is very little change in equivalent width with column (saturated) until the line becomes so optically thick that the Lorentzian wings dominate, leading to the heavily saturated increase. The point at which the line becomes saturated depends on the velocity structure. Higher turbulent velocity means that the line is broader so it remains optically thin in the core (unsaturated) up to a higher column density (dotted black line).

obvious. There are multiple ionized absorption lines which dominate the spectrum as well as photo-electric edges.

Soft X-ray absorption features, especially from H and He like Oxygen, are seen in half of type 1 Seyferts (Reynolds 1997). High resolution grating spectra from Chandra and XMM-Newton observations have shown these in some detail. Typically, the best datasets require several different column densities, each with different ionization parameter, in order to fit the data. By contrast, the BHB show little in the way of soft X-ray absorption (GROJ1655-40 is an extreme exception: Miller et al 2006a), but highly inclined systems do show H and He-like Fe $K\alpha$ absorption lines in bright states (Ueda et al. 1998; Yamaoka et al. 2001; Kotani et al. 2000; Lee et al. 2002; Kubota et al 2007).

In each case, the origin of this ionized material can be constrained by measuring the velocity width (or an upper limit on the velocity width) of a line to get the column density of that ion via a curve of growth. This can be done separately for each transition, but a better way is to take a photo-ionization code and use this to

calculate the (range of) column density and ionization state required to produce all the observed transitions assuming solar abundance ratios. The spectrum gives an estimate for L so the equation for the ionization parameter $\xi = L/nR^2$ can be inverted by writing $N_H = n\Delta R$ to give $R = L/(N_H\xi) \times (\Delta R/R)$. Since $\Delta R/R \lesssim 1$, then the distance of the material from the source is $R \lesssim L/(N_H\xi)$. A small radius means that the material is most probably launched from the accretion disc itself, probably as a wind.

1.4.4 Winds

Wherever X-rays illuminate material they can photo-ionize it. They also interact with the electrons by Compton scattering. Electrons are heated by Compton up-scattering when they interact with photons of energy $\epsilon \gtrsim \Theta$ but are cooled by Compton scattering by photons with energy $\epsilon \lesssim \Theta$. Since the illuminating spectrum is a broadband continuum, then the spectrum both heats and cools the electrons. The Compton temperature is the equilibrium temperature where heating of the electrons by Compton downscattering equals cooling by Compton upscattering. Section 1.3 shows that the mean energy shift is $\Delta\epsilon \sim 4\Theta\epsilon - \epsilon^2$, so integrating this over the photon spectrum gives the net heating which is zero at the equilibrium Compton temperature, Θ_{ic} , so $0 = \int N(\epsilon)\Delta\epsilon d\epsilon = \int N(\epsilon)(4\Theta_{ic}\epsilon - \epsilon^2)d\epsilon$. Hence

$$\Theta_{ic} = \frac{\int N(\epsilon)\epsilon^2 d\epsilon}{4 \int N(\epsilon)\epsilon d\epsilon}$$

For a photon spectrum with $\Gamma = 2.5$ between ϵ_i to ϵ_{max} this gives $\Theta_{ic} \approx \frac{1}{4}\sqrt{\epsilon_{max}\epsilon_i} \sim 2.5 \text{ keV}$ for energies spanning 1-100 keV. Alternatively, for a hard spectrum with $\Gamma = 1.5$ this is $\approx \epsilon_{max}/12$ or 8 keV. The effective upper limit to ϵ_{max} is around 100 keV as the reduction in Klein-Nishina cross-section means that higher energy photons do not interact very efficiently with the electrons.

Thus the irradiated face of the material can be heated up to this Compton temperature, giving typical velocities in the plasma of $v_{ic}^2 = 3kT_{ic}/m_p$. This is constant with distance from the source as the Compton temperature depends only on spectral shape (though the depth of the heated layer will decrease as illumination becomes weaker). This velocity is comparable to the escape velocity from the central object when $v_{ic}^2 \sim GM/R_{ic}$, defining a radius, R_{ic} , at which the Compton heated material will escape as a wind (Begelman, McKee & Shields 1983). This is driven by the pressure gradient, so has typical velocity at infinity of the sound speed $c_s^2 = kT_{ic}/m_p \sim v_{ic}^2 \sim GM/R_{ic}$. Thus the typical velocity of this thermally driven wind is the escape velocity from where it was launched.

As the source approaches Eddington, the effective gravity is reduced by a factor $(1 - L/L_{Edd})$, so the thermal wind can be launched from progressively smaller

radii as the continuum radiation pressure enhances the outflow, forming a radiation driven wind.

The Eddington limit assumes that the cross-section for interaction between photons and electrons is only due to electron scattering. However, where the material is not strongly ionized, there are multiple UV transitions, both photo-electric absorption edges and lines. This reduces the 'Eddington' limit by a factor σ_{abs}/σ_T which can be as large as 4000. This opacity is mainly in the lines, and the outflowing wind has line transitions which are progressively shifted from the rest energy to $\Delta\nu/\nu \approx v_\infty/c$. This large velocity width to the line means that its equivalent width is high, so it can absorb momentum from the line transition over a wide range in energy. This gives a UV line driven wind.

The final way to power a wind is via magnetic driving, but this difficult to constrain as it depends on the magnetic field configuration, so it is invoked only as a last resort.

Much of the 'warm absorber' systems seen in AGN have typical velocities, columns and ionization states which imply they are launched from size scales typical of the molecular torus (e.g. Blustin et al 2005). The much faster velocities of $\sim 0.1 - 0.2 c$ implied by the broad absorption lines (BAL's) seen bluewards of the corresponding emission lines in the optical/UV spectra of some Quasars are probably a UV line driven wind from the accretion disc. However, the similarly fast but much more highly ionized (H and He-like Fe) absorption systems seen in the X-ray spectra of some AGN (see ahead in Fig 1.26c and d) probably require either continuum driving with $L \sim L_{Edd}$ or magnetic driving (as the ionization state is so high that the line opacity is negligible with respect to σ_T).

By contrast, the BHB typically show fairly low outflow velocity of the highly ionized Fe $K\alpha$, mostly consistent with a thermally driven wind from the outer accretion disc (e.g. Kubota et al 2007, DGK07), although the extreme absorber seen in one observation from GRO J1655-40 may require magnetic driving (Miller et al 2006a, Kallman et al 2009). However, this does assume that the observed luminosity, L_{obs} measures the intrinsic luminosity, L_{int} . If there is electron scattering in optically thick, completely ionized material along the line of sight then $L_{obs} = e^{-\tau} L_{int} \ll L_{int}$ (Done & Davies 2008). Such scattering would strongly suppress the rapid variability power (Zdziarski et al 2010) and indeed the variability power spectra of these data lack all high frequency power above 0.3-1 Hz, rather than extending to the ~ 10 Hz seen normally (see Fig. 1.5). Thus thermal winds potentially explain all of what we see in terms of absorption from BHB.

1.5 Reflection

Wherever X-rays illuminate optically thick material such as the accretion disc the photons have some probability to scatter off an electron, and so bounce back into the line of sight. This reflection probability is set by the relative importance of scattering versus photo-electric absorption. For neutral material, photo-electric absorption dominates at low energies so the reflected fraction is very small. However, the photo-electric cross-section decreases with energy so the reflected fraction increases. Iron is the last astrophysically abundant element (due to element synthesis in stars as released in supernovae - see P. Podsiadlowski, this volume), so after 7.1 keV there are no more significant additional sources of opacity. The cross-section decreases as E^{-3} , becoming equal to σ_T at around 10 keV for solar abundance material (Fig. 1.20a). Above this, scattering dominates, leading to a more constant reflected fraction, but at higher energies, the photon energy is such that Compton downscattering is important, so the reflection is no longer elastic. Photons at high energy do reflect, but do not emerge at the same energy as they are incident. This gives a break at high energies as Compton scattering conserves photon *number*, and the number of photons is much less at higher energies. Thus neutral reflection gives rise to a very characteristic peak between 20-50 keV, termed the reflection hump, where lower energy photons are photo-electrically absorbed and higher photons are (predominantly) downscattered (Fig. 1.20b: George & Fabian 1991; Matt, Perola & Piro 1991)

The dependence on photo-electric absorption at low energies means that the spectrum is also accompanied by the associated emission lines as the excited ion with a gap in the K ($n=1$) shell decays to its ground state. This excess energy can be emitted as a fluorescence line ($K\alpha$ if it is the $n=2$ to $n=1$ transition, $K\beta$ for $n=3$ to $n=1$ etc). However, at low energies, the reflected emission forms only a very small contribution to the total spectrum, so any emission lines emitted below a few keV are strongly diluted by the incident continuum. These lines are also additionally suppressed as low atomic number elements have a higher probability to de-excite via Auger ionization, ejecting an outer electron rather than emitting the excess energy as a fluorescence line. This means that iron is the element which has most impact on the observed emission, as this is emitted where the fraction of reflected to incident spectrum is large, and has the highest fluorescence probability. All this combines to make a reflection spectrum which contains the imprint of the iron K edge and line features, as well as the characteristic continuum peak between 20-50 keV (Fig. 1.20b: George & Fabian 1991; Matt, Perola & Piro 1991).

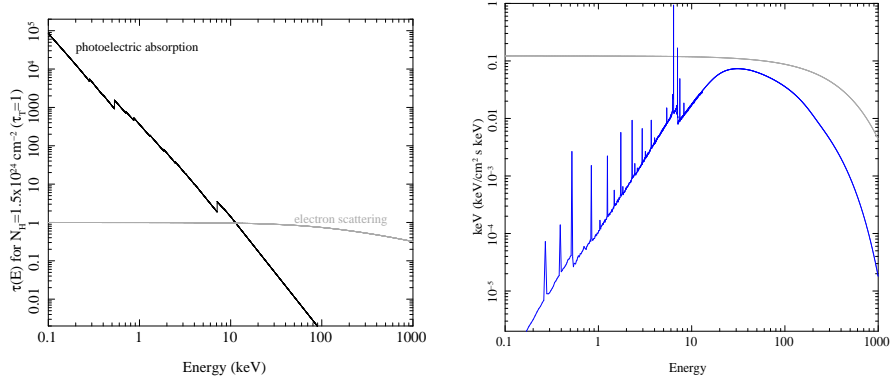


Figure 1.20 a) The absorption cross-section for neutral material with solar abundance for a column of $\tau_T = 1$ i.e. $N_H = 1.5 \times 10^{24} \text{ cm}^{-2}$ (black), together with the full (Klein-Nishima) electron scattering cross-section (grey). b) shows the corresponding reflection spectrum from such material. The much larger absorption cross-section at low energies means that most incident photons are absorbed rather than reflected, but Compton downscattering means that high energy photons are not reflected elastically. The combination of these two effects makes the characteristic peak between 20-50 keV, termed the reflection hump, with atomic features superimposed on this. Figure courtesy of M. Gilfanov.

1.5.1 Ionised Reflection

The dependence on photo-electric absorption at low energies means that reflection is sensitive to the ionization state of the reflecting material. Fig. 1.21a shows how the absorption cross-section changes as a function of ionization state using a very simple model for photoelectric absorption which considers only the photoelectric edge opacity. The progressive decrease in opacity at low energies for increased ionization state means an increase in reflectivity at these energies as shown in Fig. 1.21b for simple models of the reflected continuum (PEXRIV model in XSPEC).

However, this continuum is accompanied by emission lines and bound-free (recombination) continua and the lines can be more important for ionized material. This is due to both an increase in emissivity (He-like lines especially have a high oscillator strength) and to the fact that the increased reflected fraction at low energies mean that these lines are not so diluted by the incident continuum. Better models of ionized reflection are shown in Fig. 1.22. These include both the self consistent emission lines and recombination continua, and the effects of Compton scattering within the disc. By definition, we only see down to a depth of $\tau(E) = 1$. Thus the reflected continuum only escapes from above a depth of $\tau(E) \sim 1$. Fig. 1.20a shows that the iron line is produced in a region with $\tau_T \sim 0.5$, so a fraction $e^{-\tau_T} \sim 1/3$ of the line is scattered. For neutral material, this forms a

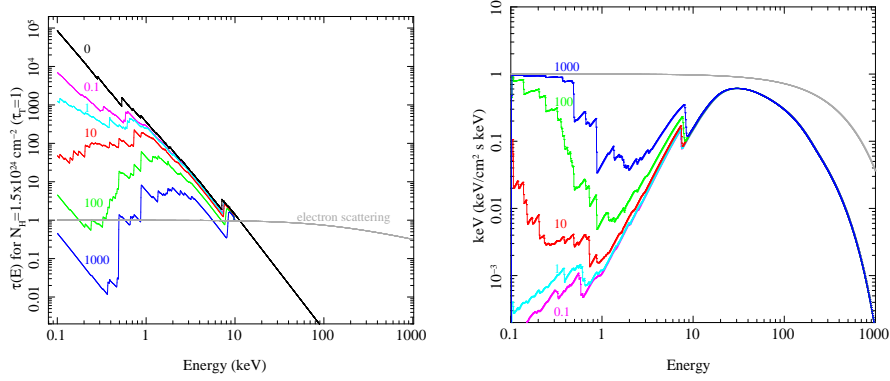


Figure 1.21 a) The ionized absorption cross-section for material with solar abundance for a column of $\tau_T = 1$ i.e. $N_H = 1.5 \times 10^{24} \text{ cm}^{-2}$. The curves are labeled with the value of ξ , and shown together with the full (Klein-Nishima) electron scattering cross-section (grey) as in Fig. 1.20 b) shows the corresponding reflection spectrum from such material. Increased ionization gives decreased opacity at low energies and hence more reflection. The reflected spectrum does not depend on photo-electric absorption at high energies, so is unchanged by ionization.

Compton downscattering shoulder to the line, but for ionized material the disc is heated by the strong irradiation up to the Compton temperature. Compton upscattering can be important as well as downscattering, so the line and edge features are broadened (Young et al 2001, see Fig. 1.22b). Models including these effects are publically available as the XSPEC ATABLE model, REFLIONX.MOD, and this should be used rather than PEXRIV for ionized reflection. However, the incident continuum for this model is an exponential power law, so this can have problems with the continuum form at high energies (see Fig. 1.9a).

1.5.2 Ionization Instability: Vertical Structure of the disc

The slab models described above assume that the irradiated material has constant density. Yet if this material is a disc, then it should be in hydrostatic equilibrium, so the density responds to the irradiation heating. The top of the disc is heated to the Compton temperature, so expands, so its density drops, so its ionization state is very high. Further into the disc, hydrostatic equilibrium means that the pressure has to increase in order to hold up the weight of the layers above. The Compton temperature remains the same, so the density has to increase, but an increase in density means an increase in importance of bremsstrahlung cooling. This pulls the temperature down further, but the pressure must increase so the density has to increase further still, so the cooling increases. Eventually the temperature/ionization state drops to low enough levels that not all the material is completely ionized. Bound

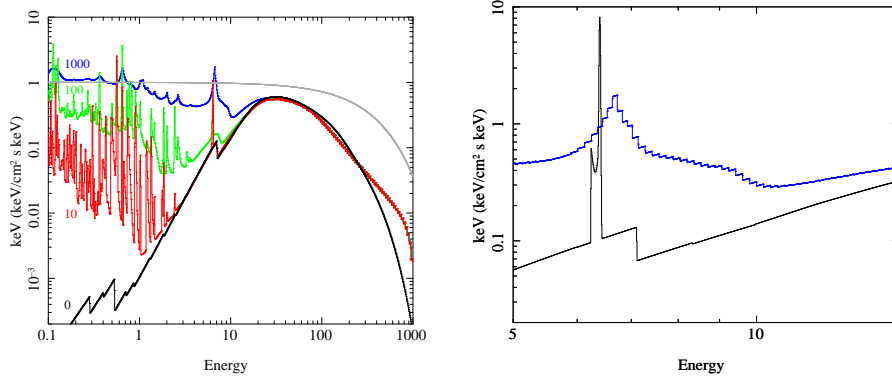


Figure 1.22 a) Ionized reflection models from a constant density slab which include the self-consistent line and recombination continuum emission. The curves are labeled with the value of ξ , and are clearly much more complex than the simple reflected continua models in Fig. 1.21. b) shows a detailed view of the iron line region. For neutral material (black), around 1/3 of the line photons are scattered in the cool upper layers of the disc before escaping, forming a Compton down-scattered shoulder to the line. Conversely, for highly ionised reflection (blue), the upper layers of the disc are heated to the Compton temperature and Compton upscattering as well as downscattering broadens the spectral features.

electrons means that line cooling can contribute, pulling the temperature down even faster, with a corresponding increase in density. The material thus makes a very rapid transition from almost completely ionized to almost completely neutral. Thus the reflection spectrum is a composite of many different ionization parameters, with some contribution from the almost completely ionized skin, and some from the almost completely neutral material underlying the instability point, but with very little reflection at intermediate ionization states (Nayakshin, Kazanas & Kallman 2000; Done & Nayakshin 2007).

The difference in Compton temperature for hard spectral illumination and soft spectral illumination only changes the ionization state of the skin. For hard illumination, the high Compton temperature gives a very low density and high ionization state so the skin is almost completely ionized as described above. For softer illumination, the Compton temperature is lower, so the density is higher and the ionization state of the skin is lower, making it highly ionised rather than completely ionized. However, there is still the very rapid transition from highly ionized to almost neutral due to the extremely rapid increase in cooling from partially ionized material (Fig. 1.23; see also Done & Nayakshin 2007). Fig. 1.24a and b shows how this very different vertical structure for temperature-density-ionization affects the expected reflection signature.

The same underlying ionization instability, but for X-ray illumination of dense,

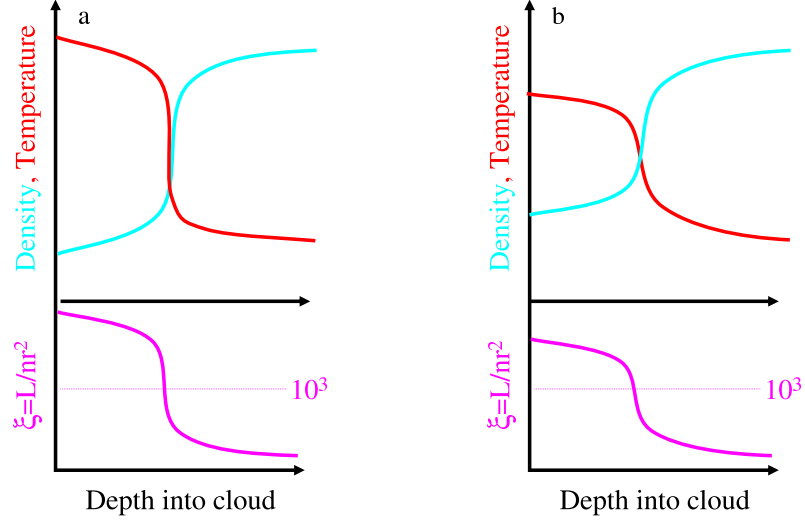


Figure 1.23 a) The ionization instability for material in hydrostatic equilibrium (or any general pressure balance) from hard spectral illumination. The high Compton temperature means that the material expands to very low density, and hence high ionization. b) shows the corresponding vertical structure from soft spectral illumination, where the lower Compton temperature gives higher surface density and hence lower ionization. Both show the rapid drop in ionization that comes from the dramatic increase in cooling from lines when partially ionized ions can exist.

cool clouds in pressure balance with a hotter, more diffuse medium (Krolik, McKee & Tarter 1981), may well be the origin of the multiple phases of ionization state seen in the AGN 'warm absorbers' (e.g. Netzer et al 2003; Chevallier et al 2006).

1.5.3 Radial Structure

This vertical structure of a disc should change with radius, giving rise to a different characteristic depth of the transition and hence a different balance between highly ionized reflection from the skin and neutral reflection from the underlying material. This does depend on the unknown source geometry as well as the initial density structure of the disc, and how it depends on radius, which in turn depends on the (poorly understood) energy release in the disc (see e.g. Nayakshin & Kallman 2001). The XION model (Nayakshin) incorporates both the vertical structure from the ionisation instability, and its radial dependence for some assumed X-ray geometry and underlying disc properties.

However, if the material is mostly neutral, then neither vertical nor radial struc-

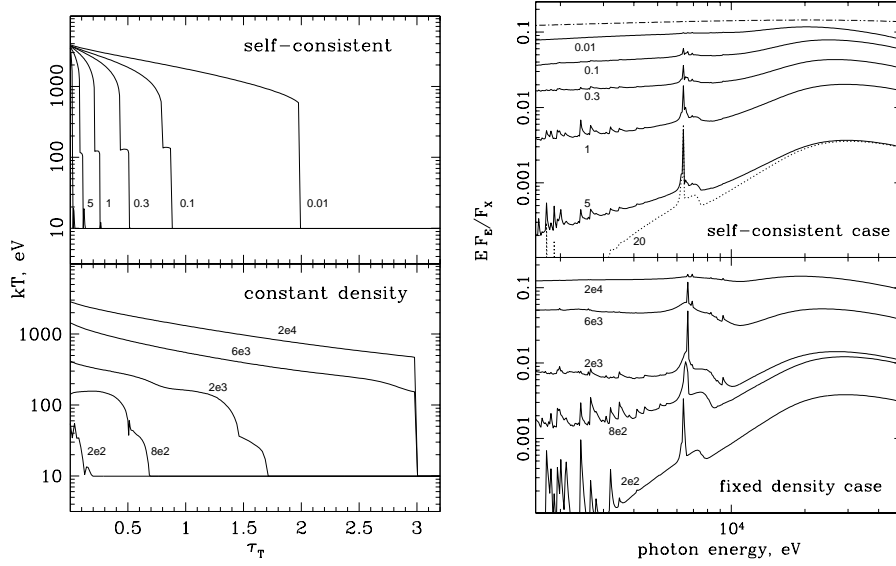


Figure 1.24 a) The vertical temperature structure from material in hydrostatic equilibrium (upper panel) shows a sharp drop in temperature due to the ionization instability. This is rather different to the much smoother drop in temperature seen for assuming the material has constant density (lower panel). b) The resulting differences in ionization structure of the disc photosphere give rise to different reflected spectra. In particular, the deep edge seen in the constant density reflected spectrum at $\xi = 2000$ is never present in the hydrostatic models (Nayakshin et al 2000).

ture gives rise to a change in the reflected spectrum with radius. Neutral material remains neutral as the illumination gets weaker, so these models are very robust.

1.5.4 Relativistic Broadening

The reflected emission from each radius has to propagate to the observer but it is emitted from material which is rapidly rotating in a strong gravitational field. There is a combination of effects which broaden the spectrum. Firstly, the line of sight velocity gives a different Doppler shift from each azimuth, with maximum blueshift from the tangent point of the disc coming towards the observer, and maximum redshift from the tangent point on the receding side. Length contraction along the direction of motion means that the emission is beamed forward, so the blueshifted material is also brightened while the redshifted side of the disc is suppressed. These effects are determined only by the component of the velocity in the line of sight, so are not important for face on discs. However, the material is intrinsically moving fast, in Keplerian rotation, so there is always time dilation (fast clocks run slow, also

sometimes termed transverse redshift as it occurs even if the velocity is completely transverse) and gravitational redshift.

All these effects decrease with increasing radius. The smaller Keplerian velocity means smaller Doppler shifts and lower boosting giving less difference between the red and blue sides of the line. The lower velocity also means less time dilation while the larger radius means less gravitational redshift. Thus larger radii give narrower lines, so the line profile is the inverse of the radial profile, with material furthest out giving the core of the line and material at the innermost orbit giving the outermost wings of the line (Fabian et al 1989; Fabian et al 2000). The relative weighting between the inner and outer parts of the line are given by the radial emissivity, where the line strength $\propto r^{-\beta}$. This gives $\beta = 3$ for either an emissivity which follows the illumination pattern from a gravitationally powered corona, or 'lamppost' point source illumination. This characteristic line profile is given by the DISKLINE (Fabian et al 1989) and LAOR (Laor 1991) models for Schwarzschild and extreme Kerr spacetimes, respectively.

However, these relativistic effects should be applied to the entire reflected continuum, not just the line. This can be modeled with the KDBLUR model (a re-coding of the LAOR model for convolution), or the newer KY models which work for any spin (Dovciak, Karas & Yaqoob 2004). Fig. 1.25a shows the REFLIONX.MOD reflection ATABLE convolved with KDBLUR for $r_{in} = 30, 6$ and $1.23R_g$ for $i = 60^\circ$. Blueshifts slightly predominate over redshifts, with the 'edge' energy (actually predominantly set by the blue wing of the line) at 7.8 keV for $r_{in} = 6$ and 1.23 (green and blue, respectively) compared to 7.1 keV for $r_{in} = 30$ (red) and in the intrinsic slab spectrum (grey). Redshifts are more important for lower inclinations. Fig. 1.25b shows a comparison of the iron line region for $i = 60^\circ$ (dotted lines) with $i = 30^\circ$ (solid lines). The 'edge' energy is now ~ 6.7 keV for both $r_{in} = 1.235$ and 6.

Relativistic smearing is harder to disentangle for ionized material as the iron features are broadened by Compton scattering so there are no intrinsically sharp features to track the relativistic effects (see Fig. 1.25c and d). Nonetheless, the energies at which the line/edge features are seen are clearly shifted.

1.5.5 Observations of reflected emission in AGN: iron line and soft X-ray excess

Reflection is seen in AGN. There is a narrow, neutral iron line and reflection continuum from illumination of the torus, and there is also a broad component from the disc. This broad component is often consistent with neutral reflection from material within $50R_g$ produced from r^{-3} illumination (Nandra et al 2007). However, a small but significant fraction of objects require much more extreme line parameters, with $r_{in} < 3R_g$, and much more centrally concentrated illumination $\propto r^{-\beta}$

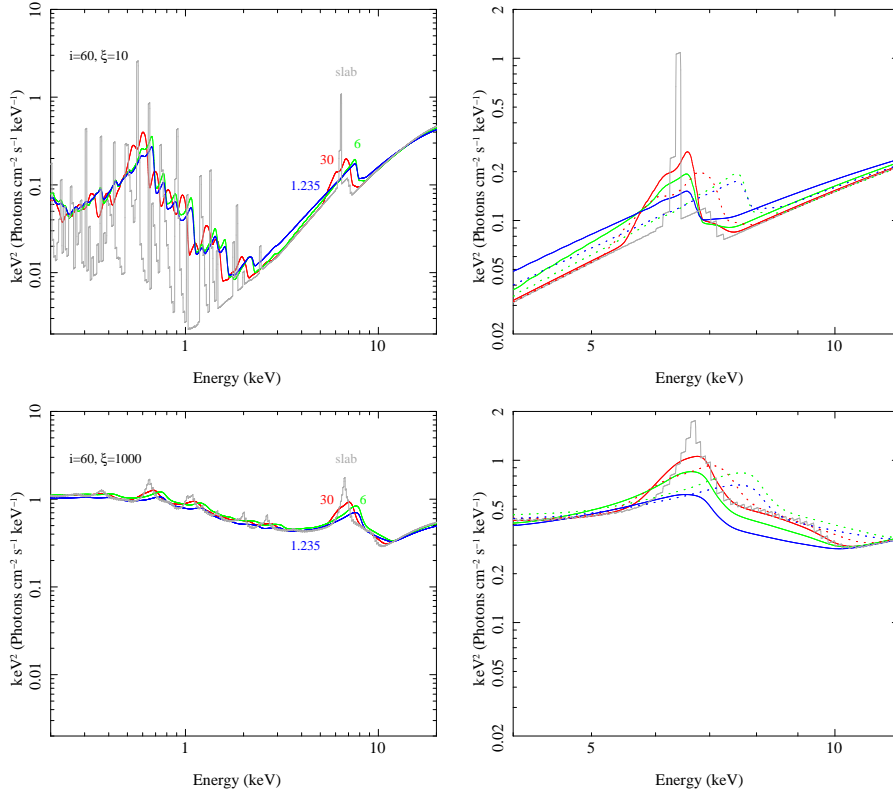


Figure 1.25 a) Relativistic smearing of reflection from a constant density slab with low ionization ($\xi = 10$) viewed at 60° . The intrinsic emission (grey) is convolved with the relativistic functions with $r_{in} = 30$ (red), 6 (green) and 1.235 (blue). b) focuses in on the iron line region to show the difference in line profile for $i = 30^\circ$ (solid lines) compared to $i = 60^\circ$ (dotted lines). c) and d) show the same for highly ionized material ($\xi = 1000$). The relativistic effects shift the shape of the become much less marked as the spectral features are intrinsically broadened by Comptonization in the strongly irradiated material.

where $\beta = 5 - 6$!!(MCG-6-30-15: Wilms et al 2001; Fabian & Vaughan 2003; 1H0707-495: Fabian et al 2002; Fabian et al 2004; NGC4051: Ponti et al 2006). These all generally high mass accretion rate objects, predominantly Narrow Line Seyfert 1s.

However, the X-ray spectrum is *not* simply made up of the power law and its reflection. There is also a 'soft X-ray excess', clearly seen in the spectra of most high mass accretion rate AGN below 1 keV. Fig. 1.26a shows the changing shape of this soft excess for different intensity sorted spectra of Mkn766. This is rather smooth, so looks like a separate continuum component. However, fitting this for a large sample of AGN gives a typical 'temperature' of this component that is remarkably

constant irrespective of mass of the black hole (Czerney et al 2003; Gierlinski & Done 2004b). This is very unlike the behaviour of a disc or any component connected to a disc, requiring some (currently unknown) 'thermostat' to maintain this temperature. Another, more subtle, problem is that 'normal' BHB do not show such a component in their spectra, so these AGN spectra do not exactly correspond to a scaled up version of the BHB high/very high states. However, there *is* such a separate component in the most luminous state of the brightest BHB GRS 1915+105 which may scale up to produce the soft excess in the most extreme AGN (Middleton et al 2009; see Fig. 1.27c).

More clues to the nature of the soft excess can come from its variability. These objects are typically highly variable, and the spectrum changes as a function of intensity in a very characteristic way. At the highest X-ray luminosities, the 2-10 keV spectrum can often be well described by a $\Gamma \sim 2.1$ power law, with resolved iron emission line, and a soft excess which is a factor ~ 2 above the extrapolated 2-10 keV power law at 0.5 keV. Conversely, at the lowest luminosities, the apparent 2-10 keV power law index is much harder (and there are absorption systems from highly ionized iron), and the soft excess above this extrapolated emission is much larger. Fig. 1.26a shows this spectral variability for Mkn 766.

The entire spectrum at the lowest luminosity looks like moderately ionized reflection (with the iron K alpha He and H like lines absorption lines superimposed), but the lack of soft X-ray lines (as well as the lack of a resolved iron emission line) means it would have to be extremely strongly distorted by relativistic effects. The classic extreme iron line source, MCG-6-30-15 has similar spectral variability but with stronger 'warm absorption' features around 0.7-1 keV and stronger ionized iron absorption lines (see Fig. 1.26b). In both these sources, most of the spectral variability can be modeled if there is an extremely relativistically smeared reflection component which remains constant, while the $\Gamma = 2.1$ power law varies, giving increasing dilution of the reflected component at high fluxes (Fabian & Vaughan 2003).

The obvious way for the reflected emission to remain constant is if it is produced by far off material, but the extreme smearing requirement conflicts with this. Instead, lightbending from a source very close to the event horizon could give both the required central concentration of the illumination pattern and apparent constancy of reflection if the variability is dominated by changes in source position giving changes in lightbending (Miniutti et al 2003; Fabian et al 2004; Miniutti & Fabian 2004). As the X-ray source gets closer to the black hole, the X-ray emission is increasingly focused onto the inner disc, and so the amount of direct emission seen drops.

However, there are some physical issues with this solution. Firstly, unlike the iron line, the soft excess requires extreme smearing (small inner radius, strongly

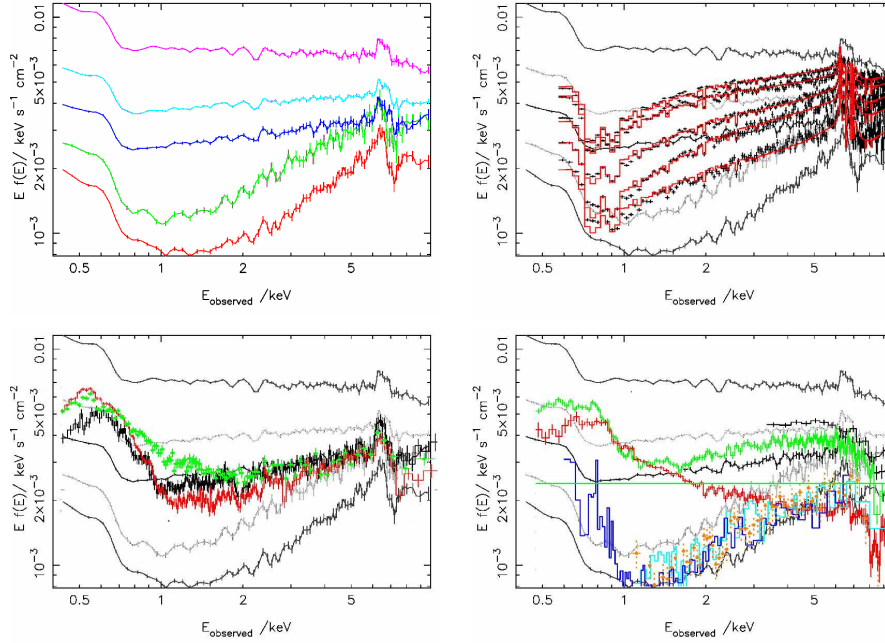


Figure 1.26 Intensity sorted spectra from a selection of high mass accretion rate AGN. a) shows Mkn766 (L. Miller et al 2007). This has a weak soft excess and soft 2–10 keV spectrum, together with a weak emission line at the highest luminosities, while the lowest flux states have a strong soft excess, hard 2–7 keV spectrum, with a strong drop above this, enhanced by strong He- and H-like absorption lines. b) shows the same for MCG-6-30-15 (L. Miller et al 2008). This shows very similar variability, though spans a smaller range. It also has a stronger ‘warm absorber’, seen by the drop at 0.7–1 keV, and stronger absorption lines of He and H-like iron on the blue wing of the line. c) shows PG1211+10, with even less range in variability but with ionized iron absorption which is strongly blueshifted (Reeves et al 2008; Pounds et al 2003) d) shows PDS456 (Reeves et al 2009), where the lowest intensity spectra look like those from MKN766, but with a stronger drop blueward of the line and even more highly blueshifted iron absorption lines. However, this can also show a rather different spectral shape, with steeper continua (red points).

centrally concentrated emissivity) in almost all the objects in order to smooth out the strong soft X-ray line emission predicted by reflection (Crummy et al 2006). Secondly, to produce the soft excess from reflection requires that the reflecting material is moderately ionized over much of the disc photosphere. Yet the ionisation instability for material in pressure balance means that only a very small fraction of the disc photosphere can be in such a partially ionised state (see section 1.5.2). Either the disc is not in hydrostatic equilibrium (held up by magnetic fields?) or the soft excess is not formed from reflection (Done & Nayakshin 2007).

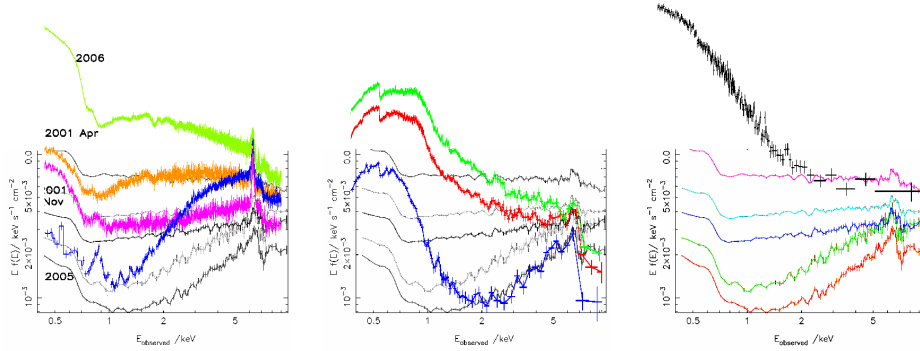


Figure 1.27 As in Fig. 1.26, with Mkn766 as background but now for objects showing somewhat different variability. a) shows NGC 3516 (Turner et al 2008). Plainly there is some contribution here from complex absorption. b) shows 1H0707-495, which has a hardest spectrum which is similar to that from Mkn766, but with an enormous drop above 7 keV (Boller et al 2002), and an extremely strong soft excess. However, the softer spectra at higher luminosity look more like the strange spectrum seen from PDS456 (Fig. 1.26d), but also have clear features from iron L emission (Fabian et al 2009). c) shows RE J1034+396 one of the strongest soft excess known, which may be a real continuum component (Middleton et al 2009).

Instead, it is possible that the soft excess is formed by partially ionised material seen in absorption through optically thin material rather than reflection from optically thick material. However, there is still the issue of the lack of the expected partially ionised lines - in absorption this time rather than from emission (see Fig. 1.17b). These could be smeared out in a similar way to reflection if the wind is outflowing (Gierlinski & Done 2004b; Middleton et al 2007), but the outflow velocities required are similarly extreme to the rotation velocities (Schurch & Done 2008; Schurch et al 2009). Even including scattering in a much more sophisticated wind outflow model shows that 'reasonable' outflow velocities are insufficient to blend the atomic features at low energies into a pseudo-continuum, though this can explain the broad iron line shape without requiring extreme relativistic smearing (Sim et al 2010).

Potentially a more plausible geometry is if the absorber is clumpy, and only partially covers the source, then there are multiple lines of sight through different columns. Any mostly neutral material gives curvature underneath the iron line, making an alternative to extreme reflection for the origin of the red wing (L. Miller et al 2007; 2008; Turner et al 2008). Such neutral material will produce an iron fluorescence line, but this line can also be absorbed, so current observations cannot yet distinguish between these two models (Yaqoob et al 2009). This much more

messy geometry perhaps gives more potential to explain the larger range of complex variability seen in some of the other high mass accretion rate AGN, as shown in Fig. 1.27a and b.

It is clearly important to find out which one of these geometries we are looking at. Either we somehow have a clean line of sight down to the very innermost regions of the disc despite it being an intense UV source which should be powering a strong wind, or we are looking through a material in strong, clumpy, wind, which has important implications for AGN feedback models, giving another way to strongly suppress nuclear star formation. These questions are currently an area of intense controversy and active research.

1.5.6 Observations of Reflected Emission and Relativistic smearing in BHB

Reflection is also seen in BHB, and here the controversy over its interpretation occurs at both low and high mass accretion rates.

The amount of reflection is determined by the solid angle subtended by the disc to the hard X-ray source i.e. the fraction of the sky that is covered by optically thick material as viewed from the hard X-ray emission region. The truncated disc models for low mass accretion rates predict that this should increase as the disc moves in towards the last stable orbit, identified with the source making a transition from the low/hard to high/soft state, while the decrease in inner disc radius means that this should also be more strongly smeared by relativistic effects. With RXTE data, the solid angle of reflection increases as expected, but the poor spectral resolution means that it is very difficult to constrain the relativistic smearing. Nonetheless, these do appear more smeared in the RXTE data (Gilfanov, Churazov & Revnivtsev 1999; Zdziarski, Lubinski & Smith 1999; Ibragimov et al 2005, Gilfanov 2010).

These results were derived assuming neutral reflection, whereas the reflected spectrum is plainly ionised in the high/soft states (e.g. Gierlinski et al 1999). While some of this ionization can be from photo-ionization by the illuminating flux, at least part of it must be due to the high disc temperature (i.e. collisional ionization: Ross & Fabian 2007). Thus the high/soft and very high state require fitting with complex ionised reflection models in order to disentangle the relativistic smearing and solid angle from the ionization state. Nonetheless, attempts at this using simplistic models of ionized reflection (PEXRIV) with the RXTE data gave fairly consistent answers. The high/soft data seemed to show that the solid angle subtended by the disc is of order unity, and the (poorly constrained) smearing gives $r_{in} \approx 6$ for emissivity fixed at $\beta = 3$, as expected from the potential geometries sketched in Fig. 1.12b (Gierlinski et al 1999, Zycki, Done & Smith 1998). By contrast, the very high state geometry discussed in section 1.3.5 required that the inner disc is covered by an optically thick corona, predicting a smaller amount of reflec-

tion and smearing, again consistent with the RXTE observations (Done & Kubota 2006).

However, the first moderate and good spectral resolution results appeared to conflict with the neat picture described above. The extent of this is best seen in Miller et al (2009), who compiled some XMM-Newton spectra of BHB (plus a few datasets from other satellites) and fit with the best current relativistically smeared, ionised reflection models (together with a power law and disc spectrum). Their Table 3 shows that all the very high state spectra ($\Gamma > 2.4$), require a large solid angle of reflection from the very inner regions of the disc, at odds with the geometry proposed from the continuum shape where an optically thick corona completely covers the cool material (Done & Kubota 2006).

There are even worse conflicts with the models for the low/hard state. The truncated disc/hot inner flow models clearly predict that the amount of relativistic smearing should be lower than in the high/soft state. However, XMM-Newton data from low/hard state observations also show a line which is so broad that the disc is required to extend down to the last stable orbit of a high spin black hole. The most famous of these is GX339-4 (Miller et al 2006b; Reis et al 2008), though this one is probably an artifact of instrumental distortion of the data due to pileup (Fig. 1.28a, Done & Diaz-Trigo 2010). However, there are other data which also show a line in the low/hard state which is so broad that the disc is required to extend down to the last stable orbit of a rapidly spinning black hole (SAX J1711.6-3808: Miller et al 2009; GRO J1655-40 and XTE J1650-500: Reis et al 2009, see also Reis et al 2010). While these are not so compelling as the (piled up) data from GX339-4, they still rule out the truncated disc/hot inner flow models for the low/hard state if the extreme broad line is the only interpretation of the spectral shape.

1.6 The nature of the low/hard state in BHB and AGN

This conflict motivates us to look again at the low/hard state in particular, especially as there are other observations which also challenge the hot inner flow/truncated disc geometry. Again, this is currently an area of intense controversy and active research.

1.6.1 Intrinsic disc emission close to the transition

The high/soft state disc dominated spectra trace out $L \propto T^4$ giving strong evidence for a constant size scale inner radius (see section 1.2.4). After the transition to the low/hard state there is still a (weak) soft X-ray component which can be seen in CCD spectra (but not in RXTE due to its low energy bandpass limit of 3 keV). This has temperature and luminosity which is consistent with the same radius as seen in

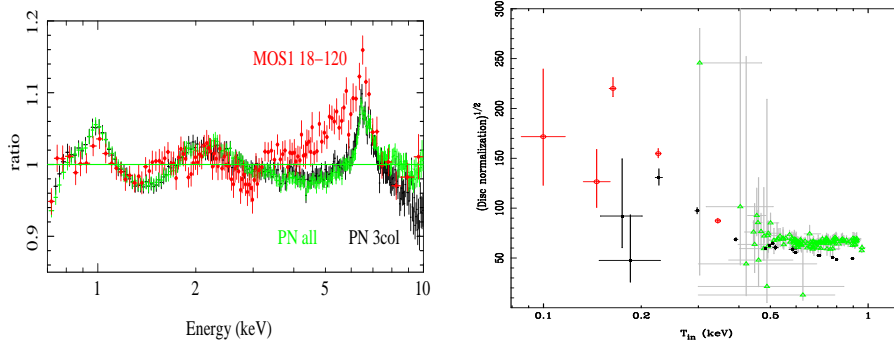


Figure 1.28 a) Residuals to a continuum model fit to the low/hard state of GX339-4. The red points show the MOS data on XMM-Newton, with an obvious, extremely broad red wing to the iron line (Miller et al 2006b). However, these data suffer from pileup, and the simultaneous PN instrument on XMM-Newton which is not piled up, show a much narrower profile (black and green data: Done & Diaz-Trigo 2010) b) Temperature versus scaled inferred inner disc radius for SWIFT (black) and RXTE (green) data from XTE J1817-330 fit to a disc plus Comptonization model. The source is in the high/soft state for temperatures above 0.4 keV, as shown by the constant radius. The two lowest temperature points at ~ 0.2 keV are low/hard states, while the ones in the 0.2–0.4 keV range are taken during the transition (intermediate state). The 3 keV lower limit to the RXTE bandpass means that it cannot follow the disc as the source goes into the transition, but the SWIFT data show that the disc radius starts to increase. A simple interpretation of the low/hard state data are that the disc returns to the last stable orbit, but the red points show how this can change by including irradiation, and the radius can be further increased to 250–300 in these units by going from a stress-free inner boundary to stress across the truncated disc edge. The disc radius cannot be unambiguously determined from the low/hard state data (Gierlinski et al (2008).

the high/soft state data, implying that the disc does not truncate (Rykoff et al 2007, Reis et al 2010).

Fig. 1.28b illustrates this with both RXTE (green) and SWIFT (black) data from the transient XTE J1817-330 (Rykoff et al 2007, Gierlinski, Done & Page 2008). The disc goes below the RXTE bandpass just as the source makes a transition from the high/soft state, but its evolution can be followed by the lower energy data from SWIFT. Plainly the SWIFT data show that the disc *does* recede during (i.e triggering!) the transition, but then in the low/hard state proper, it apparently bounces back to give the same radius as in the high/soft state. However, just after the transition, the disc is not too far recessed, so it can be strongly illuminated by the energetically dominant hard X-ray source. This changes the temperature/luminosity relation from that expected from just gravitational energy release, as shown by the red points in Fig. 1.28. Additionally, the difference in inner boundary condition (going

from the stress-free last stable orbit to a continuous stress across the truncated inner disc radius) means that the same temperature/luminosity relation implies the disc is bigger, which would move the two low/hard state points up to 250-300 in these units! This is even before taking into account that some of the disc photons are lost to our line of sight through Compton scattering if the disc underlies some of the hot inner flow. Putting these photons back into the disc gives higher luminosity/larger radii. (Makishima et al 2008).

These data show the difficulty in unambiguously reconstructing the inner radius of the disc when the disc component does not dominate the spectrum. They can be consistent with the disc down at the last stable orbit (Rykoff et al 2007; Reis et al 2010), but they can equally well be consistent with a truncated disc (Gierlinski et al 2008). However, the data during the transition are fairly clear that the disc starts to recede, so it seems most likely to me that that this continues into the low/hard state.

1.6.2 Intrinsic disc emission at very low luminosities

The transition is going to be complicated. The disc surely does not truncate in a smooth way, so there can be turbulent clumps, as well as issues with the overlap region suppressing the observed disc while also giving rise to strong illumination as discussed above. Instead, a much cleaner picture should emerge instead from a dimmer low/hard state if the disc truncates, as here it should be far from the X-ray source, so irradiation and overlap effects should be negligible. Yet there is still a weak soft X-ray component, with temperature and luminosity such that the emitting area implied is very small, of order the size scale of the last stable orbit. This has now been seen in several different CCD observations of low L/L_{Edd} sources so is clearly a robust result (Reis, Miller & Fabian 2009; Chiang et al 2009; Wilkinson & Uttley 2009)

However, putting the disc down to the last stable orbit is not a solution to these data. It is then co-spatial with the hard X-ray emission, as this must be produced on small size scales. This then runs into difficulties with reprocessing. If the hard X-ray corona overlies the optically thick disc and emits isotropically then half of the hard X-ray emission illuminates the disc. Some fraction, a , (the albedo) of this is reflected, but the remainder is thermalized in the disc and adds to its disc luminosity. The minimum disc emission is where there is no intrinsic gravitational energy release in the disc, only this reprocessed flux. This is $L_{rep} = (1 - a)L_h/2 \sim L_h/3$ as the reflection albedo cannot be high for hard spectral illumination as high energy X-rays cannot be reflected elastically. Instead they deposit their energy in the disc via Compton downscattering. Yet we see $L_{soft} \sim L_h/20$. Thus the geometry must be wrong! Either the hard X-ray source is not isotropic, perhaps beamed away from

the disc as part of the jet emission, or the material is a small ring rather than a disc so that its solid angle is much less than 2π for a full disc (Chiang et al 2009; Done & Diaz-Trigo 2010).

However, for one source, XTE J1118+480, the galactic column density is so low that there are simultaneous UV and even EUVE constraints on the spectrum (Esin et al 2001). These show that this soft X-ray component co-exists with a much more luminous, cooler UV/EUV component. If the soft X-rays are the disc, what is the UV/EUV component? Alternatively, since the UV/EUV component looks like a truncated disc, what is the soft X-ray component? It must come from a much smaller emission area than the UV/EUVE emission, and one potential origin is the inner edge (rather than top and bottom face) of the truncated disc (Chiang et al 2009). The truncation region is probably highly turbulent, so there can be intrinsic variability produced by clumps forming and shredding, as well as them reprocessing the hard X-ray irradiation. This may also explain the variability seen in this component (Wilkinson & Uttley 2009).

Thus in my opinion, none of the current observations require that there is a disc down to the last stable orbit in the low/hard state. More fundamentally, it is very difficult to make such a model not conflict with other observations. Reprocessing limits on the hardness of the spectrum requires that the X-ray source is either patchy or beamed away from the disc (Stern et al 1995; Beloborodov 1999). A patchy corona would give a reflection fraction close to unity, which is not observed even considering complex ionization of the reflected emission (Barrio et al 2003; Malzac et al 2005). Beaming naturally associates the X-ray source with the jet, but is unlikely to be able to simultaneously explain the extreme broad line parameters derived for some low/hard state sources since the illumination pattern becomes much less centrally concentrated by the beaming. I suspect that more complex continuum modelling may make these lines less extreme, but this then removes a challenge to the truncated disc as well! And unlike the beaming models, the truncated disc/hot inner flow can additionally give a mechanism for the major state transitions, and the variability.

1.7 Conclusions

The intrinsic radiation processes of blackbody radiation and Comptonization go a long way to explaining the underlying optical-to-X-ray continuum seen in both BHB and AGN. These, together with the atomic processes of absorption and reflection, and relativistic effects in strong gravity give us a toolkit with which to understand and interpret the spectra of the black hole accretion flows. This is currently an area of intense and exciting research, to try to understand accretion in

strong gravity. If you got this far, congratulations, and come and join us: we get to play around black holes!

1.8 Acknowledgements

I would like to thank the organizers of the IAC winter school for inviting me to give this series of lectures, finally giving me the motivation to write these things down. But I only know these things because of the many people who have given me their physical insight on radiation processes, especially Andy Fabian and Gabriele Ghisellini. I also thank ISAS and RIKEN for visits during which I developed some of these lectures. It also could not have been written without the 8 hours spent at Tenerife South Airport where their lack of baggage check facility put paid to my plan to spend the day at a nearby surfing beach!

References

- [] Arnaud, K.A., 1996, *Astronomical Data Analysis Software and Systems V*, eds. Jacoby G. and Barnes J., p17, ASP Conf. Series volume 101.
- [] Arévalo P., Uttley P., 2006, *MNRAS*, 367, 801
- [] Balucinska-Church M., McCammon D., 1992, *ApJ*, 400, 699
- [] Barrio F. E., Done C., Nayakshin S., 2003, *MNRAS*, 342, 557
- [] Begelman M. C., McKee C. F., Shields G. A., 1983, *ApJ*, 271, 70
- [] Belloni T. M., 2010, *LNP*, 794, 53 (arXiv:0909.2474)
- [] Beloborodov A. M., 1999, *ApJ*, 510, L123
- [] Blustin A. J., Page M. J., Fuerst S. V., Branduardi-Raymont G., Ashton C. E., 2005, *A&A*, 431, 111
- [] Boller T., et al., 2002, *MNRAS*, 329, L1
- [] Chevallier L., Collin S., Dumont A.-M., Czerny B., Mouchet M., Gonçalves A. C., Goosmann R., 2006, *A&A*, 449, 493
- [] Chiang C. Y., Done C., Still M., Godet O., 2009, *MNRAS*, in press (arXiv:0911.0287)
- [] Churazov E., Gilfanov M., Revnivtsev M., 2001, *MNRAS*, 321, 759
- [] Crummy J., Fabian A. C., Gallo L., Ross R. R., 2006, *MNRAS*, 365, 1067
- [] Coppi P. S., 1999, *ASPC*, 161, 375 (arXiv:9903158)
- [] Cunningham C. T., 1975, *ApJ*, 202, 788
- [] Czerny B., Nikołajuk M., Różańska A., Dumont A.-M., Loska Z., Zycki P. T., 2003, *A&A*, 412, 317
- [] Davis S. W., Blaes O. M., Hubeny I., Turner N. J., 2005, *ApJ*, 621, 372
- [] Davis S. W., Done C., Blaes O. M., 2006, *ApJ*, 647, 525
- [] de Martino D., Matt G., Belloni T., Haberl F., Mukai K., 2004, *A&A*, 415, 1009
- [] Di Matteo T., Celotti A., Fabian A. C., 1997, *MNRAS*, 291, 805
- [] Done C., Mulchaey J. S., Mushotzky R. F., Arnaud K. A., 1992, *ApJ*, 395, 275
- [] Done C., Magdziarz P., 1998, *MNRAS*, 298, 737
- [] Done C., Kubota A., 2006, *MNRAS*, 371, 1216
- [] Done C., Gierliński M., Kubota A., 2007, *A&ARv*, 15, 1 (DGK07)
- [] Done C., Nayakshin S., 2007, *MNRAS*, 377, L59
- [] Done C., Davis S. W., 2008, *ApJ*, 683, 389
- [] Done C., Diaz Trigo M., 2010, *MNRAS*, submitted, (arXiv:0911.3243)
- [] Dovčiak M., Karas V., Yaqoob T., 2004, *ApJS*, 153, 205
- [] Dunlop J. S., McLure R. J., Kukula M. J., Baum S. A., O’Dea C. P., Hughes D. H., 2003, *MNRAS*, 340, 1095

- [] Durant M., Gandhi P., Shahbaz T., Fabian A. P., Miller J., Dhillon V. S., Marsh T. R., 2008, *ApJ*, 682, L45
- [] Esin A. A., McClintock J. E., Narayan R., 1997, *ApJ*, 489, 865
- [] Esin A. A., McClintock J. E., Drake J. J., Garcia M. R., Haswell C. A., Hynes R. I., Munro M. P., 2001, *ApJ*, 555, 483
- [] Fabian A. C., Rees M. J., Stella L., White N. E., 1989, *MNRAS*, 238, 729
- [] Fabian A. C., Iwasawa K., Reynolds C. S., Young A. J., 2000, *PASP*, 112, 1145
- [] Fabian A. C., Ballantyne D. R., Merloni A., Vaughan S., Iwasawa K., Boller T., 2002, *MNRAS*, 331, L35
- [] Fabian A. C., Vaughan S., 2003, *MNRAS*, 340, L28
- [] Fabian A. C., Miniutti G., Gallo L., Boller T., Tanaka Y., Vaughan S., Ross R. R., 2004, *MNRAS*, 353, 1071
- [] Fabian A. C., et al., 2009, *Natur*, 459, 540
- [] Fanidakis N., Baugh C. M., Benson A. J., Bower R. G., Cole S., Done C., Frenk C. S., 2010, *MNRAS*, submitted, (arXiv:0911.1128)
- [] Gandhi P., et al., 2008, *MNRAS*, 390, L29
- [] Gammie C. F., Shapiro S. L., McKinney J. C., 2004, *ApJ*, 602, 312
- [] George I. M., Fabian A. C., 1991, *MNRAS*, 249, 352
- [] Gierliński M., Zdziarski A. A., Poutanen J., Coppi P. S., Ebisawa K., Johnson W. N., 1999, *MNRAS*, 309, 496
- [] Gierliński M., Done C., 2003, *MNRAS*, 342, 1083
- [] Gierliński M., Done C., 2004a, *MNRAS*, 347, 885
- [] Gierliński M., Done C., 2004b, *MNRAS*, 349, L7
- [] Gierliński M., Zdziarski A. A., 2005, *MNRAS*, 363, 1349
- [] Gierliński M., Done C., Page K., 2008, *MNRAS*, 388, 753
- [] Gilfanov M., Churazov E., Revnivtsev M., 1999, *A&A*, 352, 182
- [] Gilfanov M., 2010, *LNP*, 794, 17 (arXiv:0909.2567v1)
- [] Ghisellini G., 1989, *MNRAS*, 236, 341
- [] Gladstone J., Done C., Gierliński M., 2007, *MNRAS*, 378, 13
- [] Gou, L., et al. 2009, *ApJ*, 701, 1076
- [] Gou, L., McClintock, J. E., Steiner, J. F., Narayan, R., Cantrell, A. G., Bailyn, C. D., & Orosz, J. A. 2010, *ApJ*, in press (arXiv:1002.2211)
- [] Haardt F., Maraschi L., 1993, *ApJ*, 413, 507
- [] Hynes R. I., Brien K. O., Mullally F., Ashcraft T., 2009, *MNRAS*, 399, 281
- [] Ibragimov A., Poutanen J., Gilfanov M., Zdziarski A. A., Shrader C. R., 2005, *MNRAS*, 362, 1435
- [] Ingram A., Done C., Fragile P. C., 2009, *MNRAS*, 397, L101
- [] Ingram A., Done C., 2010, *MNRAS*, in press (arXiv:0907.5485)
- [] Juett A. M., Schulz N. S., Chakrabarty D., 2004, *ApJ*, 612, 308
- [] Kallman T., Bautista M., 2001, *ApJS*, 133, 221
- [] Kallman T. R., Palmeri P., Bautista M. A., Mendoza C., Krolik J. H., 2004, *ApJS*, 155, 675
- [] Kallman T. R., Bautista M. A., Goriely S., Mendoza C., Miller J. M., Palmeri P., Quinet P., Raymond J., 2009, *ApJ*, 701, 865
- [] Kanbach G., Straubmeier C., Spruit H. C., Belloni T., 2001, *Natur*, 414, 180
- [] King A. R., Kolb U., 1999, *MNRAS*, 305, 654
- [] King A. R., Pringle J. E., Livio M., 2007, *MNRAS*, 376, 1740
- [] Kolehmainen M., Done C., 2009, *MNRAS*, submitted, (arXiv:0911.3281)
- [] Kotov O., Churazov E., Gilfanov M., 2001, *MNRAS*, 327, 799
- [] Körtling E. G., Jester S., Fender R., 2006, *MNRAS*, 372, 1366

- [] Kotani T., Ebisawa K., Dotani T., Inoue H., Nagase F., Tanaka Y., Ueda Y., 2000, *ApJ*, 539, 413
- [] Krolik J. H., McKee C. F., Tarter C. B., 1981, *ApJ*, 249, 422
- [] Kubota A., Makishima K., Ebisawa K., 2001, *ApJ*, 560, L147
- [] Kubota A., Done C., 2004, *MNRAS*, 353, 980
- [] Kubota A., et al., 2007, *PASJ*, 59, 185
- [] Kubota A., Done C., Davis S.W., Dotani T., Mizuno T., Ueda Y., 2010, *ApJ*, in press (arXiv:1003.3350)
- [] Laor A., 1991, *ApJ*, 376, 90
- [] Lee J. C., Reynolds C. S., Remillard R., Schulz N. S., Blackman E. G., Fabian A. C., 2002, *ApJ*, 567, 1102
- [] Li L.-X., Zimmerman E. R., Narayan R., McClintock J. E., 2005, *ApJS*, 157, 335
- [] Liu B. F., Yuan W., Meyer F., Meyer-Hofmeister E., Xie G. Z., 1999, *ApJ*, 527, L17
- [] Lyubarskii Y. E., 1997, *MNRAS*, 292, 679
- [] Maccarone T. J., 2003, *A&A*, 409, 697
- [] Malzac J., Dumont A. M., Mouchet M., 2005, *A&A*, 430, 761
- [] Malzac J., Belmont R., 2009, *MNRAS*, 392, 570
- [] Makishima K., et al., 2008, *PASJ*, 60, 585
- [] Matt G., Perola G. C., Piro L., 1991, *A&A*, 247, 25
- [] Mayer M., Pringle J. E., 2007, *MNRAS*, 376, 435
- [] McClintock J. E., Shafee R., Narayan R., Remillard R. A., Davis S. W., Li L.-X., 2006, *ApJ*, 652, 518
- [] McConnell M. L., et al., 2002, *ApJ*, 572, 984
- [] Middleton M., Done C., Gierliński M., Davis S. W., 2006, *MNRAS*, 373, 1004
- [] Middleton M., Done C., Gierliński M., 2007, *MNRAS*, 381, 1426
- [] Middleton M., Done C., Ward M., Gierliński M., Schurch N., 2009, *MNRAS*, 394, 250
- [] Miller J. M., Raymond J., Fabian A., Steeghs D., Homan J., Reynolds C., van der Klis M., Wijnands R., 2006a, *Natur*, 441, 953
- [] Miller J. M., Homan J., Steeghs D., Rupen M., Hunstead R. W., Wijnands R., Charles P. A., Fabian A. C., 2006b, *ApJ*, 653, 525
- [] Miller J. M., Reynolds C. S., Fabian A. C., Miniutti G., Gallo L. C., 2009, *ApJ*, 697, 900
- [] Miller L., Turner T. J., Reeves J. N., George I. M., Kraemer S. B., Wingert B., 2007, *A&A*, 463, 131
- [] Miller L., Turner T. J., Reeves J. N., 2008, *A&A*, 483, 437
- [] Miniutti G., Fabian A. C., Goyder R., Lasenby A. N., 2003, *MNRAS*, 344, L22
- [] Miniutti G., Fabian A. C., 2004, *MNRAS*, 349, 1435
- [] Miyamoto S., Kitamoto S., Hayashida K., Egoshi W., 1995, *ApJ*, 442, L13
- [] Motch C., Ilovaisky S. A., Chevalier C., Angebault P., 1985, *SSRv*, 40, 219
- [] Nandra K., O'Neill P. M., George I. M., Reeves J. N., 2007, *MNRAS*, 382, 194
- [] Narayan R., Yi I., 1995, *ApJ*, 452, 710
- [] Nayakshin S., Kazanas D., Kallman T. R., 2000, *ApJ*, 537, 833
- [] Nayakshin S., Kallman T. R., 2001, *ApJ*, 546, 406
- [] Netzer H., et al., 2003, *ApJ*, 599, 933
- [] Nowak M. A., 1995, *PASP*, 107, 1207
- [] Ponti G., Miniutti G., Cappi M., Maraschi L., Fabian A. C., Iwasawa K., 2006, *MNRAS*, 368, 903
- [] Pounds K. A., Reeves J. N., King A. R., Page K. L., O'Brien P. T., Turner M. J. L., 2003, *MNRAS*, 345, 705
- [] Poutanen J., Svensson R., 1996, *ApJ*, 470, 249

- Pszota G., Zhang H., Yuan F., Cui W., 2008, MNRAS, 389, 423
- Reeves J., Done C., Pounds K., Terashima Y., Hayashida K., Anabuki N., Uchino M., Turner M., 2008, MNRAS, 385, L108
- Reeves J. N., et al., 2009, ApJ, 701, 493
- Reis R. C., Fabian A. C., Ross R. R., Miniutti G., Miller J. M., Reynolds C., 2008, MNRAS, 387, 1489
- Reis R. C., Fabian A. C., Ross R. R., Miller J. M., 2009, MNRAS, 395, 1257
- Reis R. C., Miller J. M., Fabian A. C., 2009, MNRAS, 395, L52
- Reis R. C., Fabian A. C., Miller J. M., 2010, MNRAS, 402, 836
- Remillard R. A., McClintock J. E., 2006, ARA&A, 44, 49
- Reynolds C. S., 1997, MNRAS, 286, 513
- Ross R. R., Fabian A. C., 2007, MNRAS, 381, 1697
- Różańska A., Czerny B., 2000, A&A, 360, 1170
- Rykoff, E. S., Miller, J. M., Steeghs, D., & Torres, M. A. P. 2007, ApJ, 666, 1129
- Schnittman, J. D., Homan, J., & Miller, J. M. 2006, ApJ, 642, 420
- Schurch, N. J., & Done, C. 2008, MNRAS, 386, L1
- Schurch N. J., Done C., Proga D., 2009, ApJ, 694, 1
- Shafee, R., McClintock, J. E., Narayan, R., Davis, S. W., Li, L.-X., & Remillard, R. A. 2006, ApJL, 636, L113
- Shakura, N. I., & Sunyaev, R. A. 1973, A&A, 24, 337
- Shimura, T., & Takahara, F. 1995, ApJ, 445, 780
- Sim, S.A., Miller, L., Long, K.S., Turner, T.J., Reeves J.N., 2010, MNRAS, in press (arXiv:1002.0544)
- Steiner, J. F., Narayan, R., McClintock, J. E., & Ebisawa, K. 2009, PASP, 121, 1279
- Stern, B. E., Poutanen, J., Svensson, R., Sikora, M., & Begelman, M. C. 1995, ApJL, 449, L13
- Titarchuk, L. 1994, ApJ, 434, 570
- Turner, T. J., Reeves, J. N., Kraemer, S. B., & Miller, L. 2008, A&A, 483, 161
- Ueda, Y., Inoue, H., Tanaka, Y., Ebisawa, K., Nagase, F., Kotani, T., & Gehrels, N. 1998, ApJ, 492, 782
- Uttley, P., & McHardy, I. M. 2001, MNRAS, 323, L26
- Uttley, P., McHardy, I. M., & Vaughan, S. 2005, MNRAS, 359, 345
- Uttley, P., 2007, ASPC, 373, 149
- van Paradijs, J. 1996, ApJL, 464, L139
- Vasudevan, R. V., & Fabian, A. C. 2007, MNRAS, 381, 1235
- Wardziński, G., & Zdziarski, A. A. 2000, MNRAS, 314, 183
- Wilkinson, T., & Uttley, P. 2009, MNRAS, 397, 666
- Wilms, J., Allen, A., & McCray, R. 2000, ApJ, 542, 914
- Wilms, J., Reynolds, C. S., Begelman, M. C., Reeves, J., Molendi, S., Staubert, R., & Kendziorra, E. 2001, MNRAS, 328, L27
- Yamaoka, K., Ueda, Y., Inoue, H., Nagase, F., Ebisawa, K., Kotani, T., Tanaka, Y., & Zhang, S. N. 2001, PASJ, 53, 179
- Yaqoob, T., Murphy, K. D., Miller, L., & Turner, T. J. 2010, MNRAS, 401, 411
- Young A. J., Fabian A. C., Ross R. R., Tanaka Y., 2001, MNRAS, 325, 1045
- Yu, W., & Yan, Z. 2009, ApJ, 701, 1940
- Zdziarski, A. A., Johnson, W. N., & Magdziarz, P. 1996, MNRAS, 283, 193
- Zdziarski A. A., Lubinski P., Smith D. A., 1999, MNRAS, 303, L11
- Zdziarski, A. A., Misra, R., & Gierliński, M. 2010, MNRAS, 402, 767
- Zhang, S. N., Cui, W., & Chen, W. 1997, ApJL, 482, L155
- Zycki, P. T., Done, C., & Smith, D. A. 1998, ApJL, 496, L25

- [1] Zycki, P. T., Done, C., & Smith, D. A. 1999, MNRAS, 305, 231